

# Understanding the complex metallic element Mn.

## I. Crystalline and noncollinear magnetic structure of $\alpha$ -Mn

D. Hobbs, J. Hafner, and D. Spišák

*Institut für Materialphysik and Center for Computational Materials Science, Universität Wien, Sensengasse 8/12, A-1090 Wien, Austria*

(Received 11 July 2002; revised manuscript received 21 January 2003; published 8 July 2003)

Manganese is an element with outstanding structural and magnetic properties. While most metallic elements adopt a simple crystal structure and order magnetically—if at all—in a simple ferromagnetic or antiferromagnetic configuration, the stable phase of manganese at ambient conditions, paramagnetic  $\alpha$ -Mn, adopts a complex crystal structure with 58 atoms in the cubic cell. At a Néel temperature of  $T_N=95$  K, a transition to a complex noncollinear antiferromagnetic phase takes place. The magnetic phase transition is coupled to a tetragonal distortion of the crystalline structure. In this paper we present an *ab initio* spin-density functional study of the structural and magnetic properties of  $\alpha$ -Mn. It is shown that the strange properties of Mn arise from conflicting tendencies to simultaneously maximize according to Hund's rule the magnetic spin moment and the bond strength, as expected for a half-filled  $d$  band. Short interatomic distances produced by strong bonding tend to quench magnetism. The crystal structure of  $\alpha$ -Mn is essentially a consequence of these conflicting tendencies—it may be considered as a topologically close-packed intermetallic compound formed by strongly magnetic (MnI, MnII) and weakly magnetic (MnIII) or even nearly nonmagnetic (MnIV) atoms. The noncollinear magnetic structure is due to the fact that the MnIV atoms arranged on triangular faces of the coordination polyhedra are not entirely nonmagnetic—their frustrated antiferromagnetic coupling leads to the formation of a local spin structure reminiscent of the Néel structure of a frustrated triangular antiferromagnet. Consequently, also the other magnetic moments are rotated out of their collinear orientation. The calculated crystalline and magnetic structures are in good agreement with experiment. However, it is suggested that the magnetism leads to a splitting of the crystallographically inequivalent sites into a larger number of magnetic subgroups than deduced from the magnetic neutron diffraction data, but in accordance with NMR experiments. In a companion paper, the properties of the other polymorphs of Mn and their relative stability will be discussed.

DOI: 10.1103/PhysRevB.68.014407

PACS number(s): 75.25.+z, 61.66.Bi, 75.50.Ee, 61.50.Ah

### I. INTRODUCTION

From the point of view of its structural and magnetic properties, Mn can be considered as the most complex of all metallic elements. As a group VII element Mn would be expected, according to the regular structural trends in the series of the  $4d$  and  $5d$  transition metals, to crystallize in a hexagonal close-packed (hcp)  $A3$  structure.<sup>1,2</sup> It is well known, however, that the magnetism of the  $3d$  elements disturbs this regular structural sequence. While for Fe and Co magnetism merely stabilizes the body-centered cubic (bcc)  $A2$  and the hcp  $A3$  structure, respectively, instead of the hcp  $A3$  and face-centered cubic (fcc)  $A1$  structures of the  $4d$  and  $5d$  homologues, Mn behaves in a totally different way.  $\alpha$ -Mn, the most stable polymorph under normal conditions of temperature and pressure has an exotic crystal structure containing 58 atoms in a cubic unit cell (Structure Report symbol  $A12$ , Pearson symbol  $cI58$ , space group  $T_d^3-I\bar{4}3m$ ),<sup>3</sup> see Fig. 1.  $\beta$ -Mn exists in the temperature interval from 1000 to 1368 K and is simple cubic with twenty atoms per unit cell ( $A13$  structure, space group  $P4_132$ ).<sup>4,5</sup> The fcc  $\gamma$ -phase is found in the high-temperature region between 1368 and 1406 K, at higher temperatures up to the melting point of  $T_M=1517$  K the  $\delta$  phase has the bcc structure. By quenching  $\gamma$ -Mn to room temperature, it can be stabilized in a face-centred-tetragonal (fct)  $A5$  structure. With the addition of

5% Cu, the tetragonal distortion can be made to disappear and structure of the quenched  $\gamma$  phase is fcc.<sup>6</sup> Recent high-pressure studies<sup>7</sup> found a structural phase transition from  $\alpha$ -Mn to an as yet not completely characterized phase. On the basis of a new diffraction peak appearing above the transition pressure of 165 GPa, it has been suggested that the new phase might be bcc, but on the basis of density functional calculations it was argued that the high-pressure phase  $\epsilon$ -Mn is hcp, in agreement with the stable crystal structures of Tc and Re.<sup>8</sup>

Magnetic ordering adds to the bewildering structural complexity of Mn.  $\alpha$ -Mn, fct  $\gamma$ -Mn, and the quenched fcc phase are antiferromagnets with Néel temperatures of  $T_N=95$ ,<sup>1,2,9</sup> 570, and 450 K,<sup>6</sup> respectively. While the magnetic structures of fcc and fct Mn are simple (planes perpendicular to the  $z$  axis are ferromagnetically polarized, the sign of the polarization alternates from one plane to the next, type-I antiferromagnetism), the magnetic transition of  $\alpha$ -Mn is coupled to a tetragonal distortion. Neutron diffraction data<sup>9-14</sup> indicate that the magnetic structure is antidy-centered (space group  $I\bar{4}2m$ ) leading to an increase of the crystallographically inequivalent atomic positions from 4 to 6.<sup>14</sup> The different atomic sites are also magnetically inequivalent: neutron-scattering data,<sup>9-14</sup> magnetic torque measurements,<sup>15</sup> and nuclear magnetic resonance (NMR) investigations<sup>16</sup> have been interpreted in terms of a noncollinear antiferromagnetic

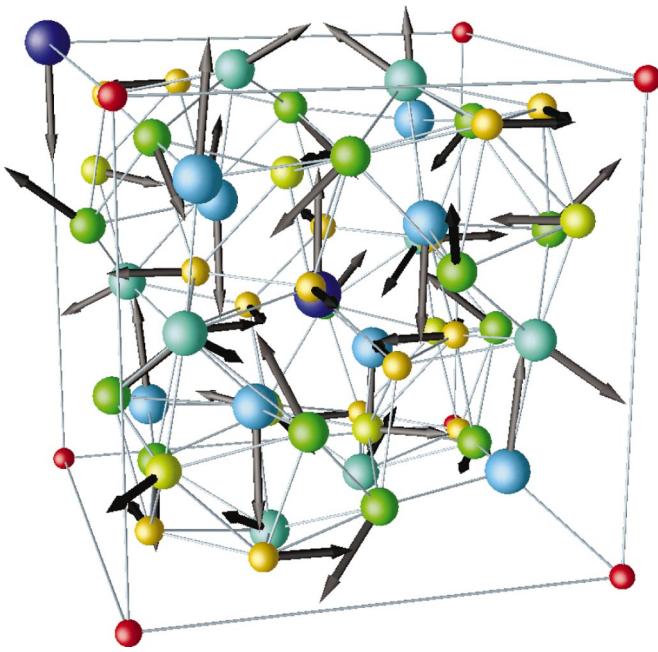


FIG. 1. (Color) Crystalline and magnetic structure of antiferromagnetic  $\alpha$ -Mn. Atomic positions in the full cubic (tetragonal) unit cell and magnitude and directions of the magnetic moments are shown. Atoms on crystallographically inequivalent sites are marked by different colors: dark blue: MnI, light blue: MnII, green and turquoise: MnIII (a) and (b), yellow and yellow-green: MnIV (a) and (b). The length of the arrows is proportional to the calculated magnetic moment, their directions indicate the orientations of the moments in the optimized magnetic structure. The magnetic moment on the MnI site has been aligned parallel to the (001) direction. The limits of the unit cell are marked by the red dots connected by straight lines, nearest-neighbor connections are also drawn.

structure with large magnetic moments on sites I and II and much smaller moments on the remaining positions—sites IVa and IVb could be occupied even by nonmagnetic Mn atoms. The details of the antiferromagnetic structure, however, depend considerably on the assumptions made for the magnetic form factors of the Mn atoms occupying the various sites—evidently high- and low-spin sites could display very different form factors. One explanation for the stability of the  $\alpha$ -Mn structure postulates indeed that the Mn atoms with different magnetic and electronic configurations behave similar to atoms with different sizes<sup>17</sup>—a point of view which is suggested by the analogy of the  $\alpha$ -Mn and the  $\chi$ -phase structures (adopted, e.g., by intermetallic compounds such as  $\text{Al}_{12}\text{Mg}_{17}$  or  $\text{Fe}_{36}\text{Cr}_{12}\text{Mo}_{10}$ ).

The properties of  $\beta$ -Mn are hardly less complex. In the simple cubic cell there are two inequivalent sites.<sup>4</sup> Nakamura *et al.*<sup>18</sup> have shown recently that  $\beta$ -Mn remains magnetically disordered down to the lowest temperatures (1.4 K) and exhibits strong spin fluctuations. Canals and Lacroix<sup>19</sup> have pointed out that the behavior of  $\beta$ -Mn is very similar to that of compounds with fully frustrated lattices (such as the *kagomé* or pyrochlore lattices) where the frustration overcomes any magnetic ordering and suggests that it should be considered as a spin liquid. The magnetic characterization of

$\beta$ -Mn using nuclear magnetic resonance<sup>18</sup> has shown that type-I sites are essentially nonmagnetic, only type-II atoms carrying paramagnetic moments. Even an only modest doping with Al drives a transition from a spin liquid to an unconventional spin-glass-like ground state.

While the structural and magnetic properties of the ferromagnetic metals Fe, Co, and Ni are now thoroughly well explained on the basis of local-spin-density (LSD) theory including generalized gradient corrections (GGC's) (see, e.g., Moroni *et al.*,<sup>20</sup> and references therein), the incommensurate spin-density-wave ground state of bcc Cr (Refs. 21,22) and the complex magnetic configurations of  $\alpha$ - and  $\beta$ -Mn continue to defy theoreticians. For the simpler  $\gamma$ ,  $\delta$ , and  $\epsilon$  phases, *ab initio* LSD calculations of phase stabilities and magnetic properties yield good agreement with experiment on samples produced by quenching or epitaxial growth if GGC's are included in the exchange-correlation functional,<sup>8,23,24</sup> Oguchi and Freeman<sup>25</sup> could even demonstrate that the tetragonal distortion observed in  $\gamma$ -Mn is magnetically driven. An important result is the evidence for a competition between high- and low-spin states in these phases. For  $\alpha$ - and  $\beta$ -Mn, however, LSD investigations have been restricted to calculations of the collinear antiferromagnetic structures at the experimental density and crystal structure.<sup>26–28</sup> A high-spin state of the Mn atoms at sites I and II, and a marginally magnetic character of those on sites III and IV is predicted in agreement with experiment, but nothing could be said about phase stability and the correlation between the magnetic and geometric structures. On the basis of a semiempirical tight-binding method and a Hubbard-type exchange Hamiltonian, Süß and Krey<sup>29</sup> have calculated both collinear and noncollinear magnetic structures for  $\alpha$ -Mn. Beyond a critical value of the intra-atomic Coulomb potential  $U$ , the collinear calculations converged to high moments on sites I and II, somewhat smaller moments on sites III, and almost nonmagnetic type-IV atoms. For the noncollinear calculations, no complete convergence could be obtained, but nevertheless an interesting result emerged: For the type III and IV atoms not two (as suggested on the basis of the analysis of the experimental data), but three magnetic subclasses have been found. This could indicate that the true magnetic structure is even more complex than suggested so far.

Due to the recent progress in LSD theory, even very complex crystalline and magnetic structures can now be computed with high accuracy. Modern plane-wave based techniques [using either ultrasoft pseudopotentials<sup>30,31</sup> or projector-augmented-waves (PAW's)<sup>32,33</sup>] allow to calculate analytically the Hellmann-Feynman forces acting on the atoms and the stresses acting on the unit cell. This enables a dynamic or static optimization of very complex crystal structures (even structures considerably more complex than  $\alpha$ -Mn have been treated<sup>34</sup>) and *ab initio* molecular-dynamics simulations of molten or glassy materials.<sup>35,36</sup> Noncollinear magnetic structures can now be treated at various levels of sophistication: (i) within an atomic-sphere approximation, the spin-density has spherical symmetry within the overlapping atomic spheres, within each sphere the direction of the magnetic moment is fixed;<sup>37,38</sup> (ii) within a full-potential linear-

TABLE I. Crystallographic information on the nonmagnetic bcc and the antiferromagnetic tetragonal phases of  $\alpha$ -Mn: space-group and atomic positions.

(a) Nonmagnetic $\alpha$ -Mn, Space group $T_d^3-I\bar{4}3m$ .		
$a = 8.865 \text{ \AA}$ (expt.), <sup>a</sup> $8.532 \text{ \AA}$ (theory).		
Atom	Number	Internal coordinates
MnI	2	$(0,0,0), (\frac{1}{2}, \frac{1}{2}, \frac{1}{2})$
MnII	8	$[(x,x,x), (x,-x,-x), (-x,x,-x), (-x,-x,-x)] + [(0,0,0); (\frac{1}{2}, \frac{1}{2}, \frac{1}{2})]$ $x(\text{II})=0.317$ (expt.) <sup>a</sup> $x(\text{II})=0.3176$ (theory)
MnIII	24	$[(x,x,z), (x,-x,-z), (-x,x,-z), (-x,-x,z)] + \text{cyclic permutations}] + [(0,0,0); (\frac{1}{2}, \frac{1}{2}, \frac{1}{2})]$ $x(\text{III})=0.357$ , $z(\text{III})=0.034$ (expt.) <sup>a</sup> $x(\text{III})=0.3563$ , $z(\text{III})=0.0372$ (theory)
MnIV	24	$[(x,x,z), (x,-x,-z), (-x,x,-z), (-x,-x,z)] + \text{cyclic permutations}] + [(0,0,0); (\frac{1}{2}, \frac{1}{2}, \frac{1}{2})]$ $x(\text{IV})=0.089$ , $z(\text{IV})=0.282$ (expt.) <sup>a</sup> $x(\text{IV})=0.0883$ , $z(\text{IV})=0.2810$ (theory)
(b) Antiferromagnetic $\alpha$ -Mn, Space group $I\bar{4}2m$ .		
$a = 8.877 \text{ \AA}$ (expt.), <sup>b</sup> $8.669 \text{ \AA}$ (theory); $c = 8.873$ (expt.), <sup>b</sup> $8.668 \text{ \AA}$ (theory).		
Axial ratio: $0.99955$ (expt.), <sup>b</sup> $0.9999$ (theory).		
Atom	Number	Internal coordinates
MnI	2	$(0,0,0), (\frac{1}{2}, \frac{1}{2}, \frac{1}{2})$
MnII	8	$[(x,x,z), (x,-x,-z), (-x,x,-z), (-x,-x,z)] + [(0,0,0); (\frac{1}{2}, \frac{1}{2}, \frac{1}{2})]$ $x(\text{II})=0.3192$ , $z(\text{II})=0.3173$ (expt.) <sup>b</sup> $x(\text{II})=0.320$ , $z(\text{II})=0.319$ (theory)
MnIIIa	8	$[(x,x,z), (x,-x,-z), (-x,x,-z), (-x,-x,z)] + [(0,0,0); (\frac{1}{2}, \frac{1}{2}, \frac{1}{2})]$ $x(\text{IIIa})=0.3621$ , $z(\text{IIIa})=0.0408$ (expt.) <sup>b</sup> $x(\text{IIIa})=0.355$ , $z(\text{IIIa})=0.032$ (theory)
MnIIIb	16	$[(x,y,z), (x,-y,-z), (-x,y,-z), (-x,-y,z), (y,x,z), (y,-x,-z), (-y,-x,-z), (-y,-x,z)] + [(0,0,0); (\frac{1}{2}, \frac{1}{2}, \frac{1}{2})]$ $x(\text{IIIb})=0.3533$ , $y(\text{IIIb})=0.0333$ , $z(\text{IIIb})=0.3559$ (expt.) <sup>b</sup> $x(\text{IIIb})=0.355$ , $y(\text{IIIb})=0.033$ , $z(\text{IIIb})=0.354$ (theory)
MnIVa	8	$[(x,x,z), (x,-x,-z), (-x,x,-z), (-x,-x,z)] + [(0,0,0); (\frac{1}{2}, \frac{1}{2}, \frac{1}{2})]$ $x(\text{IVa})=0.0921$ , $z(\text{IVa})=0.2790$ (expt.) <sup>b</sup> $x(\text{IVa})=0.088$ , $z(\text{IVa})=0.283$ (theory)
MnIVb	16	$[(x,y,z), (x,-y,-z), (-x,y,-z), (-x,-y,z), (y,x,z), (y,-x,-z), (-y,-x,-z), (-y,-x,z)] + [(0,0,0); (\frac{1}{2}, \frac{1}{2}, \frac{1}{2})]$ $x(\text{IVb})=0.0895$ , $y(\text{IVb})=0.2850$ , $z(\text{IVb})=0.0894$ (expt.) <sup>b</sup> $x(\text{IVb})=0.088$ , $y(\text{IVb})=0.283$ , $z(\text{IVb})=0.087$ (theory)

<sup>a</sup>Yamada, Ref. 13, lattice constant extrapolated to  $T=0$  K.

<sup>b</sup>Lawson *et al.*, Ref. 14 (Neutron diffraction).

ized augmented-plane-wave (FLAPW) approach,<sup>39</sup> the quantization axis is fixed only within the almost touching muffin-tin spheres, magnetization density and exchange field are described as vector fields in the interstitial region,<sup>40</sup> and (iii) PAW (Refs. 32,33) and FLAPW approaches allow for a fully unconstrained vector-field description of noncollinear magnetism.<sup>41,42</sup>

The present work is devoted to an ab initio LSD investigation of the crystalline and magnetic structures of all known phases of Mn. In the first part we present a detailed study of the crystalline and noncollinear magnetic structures of  $\alpha$ -Mn, a forthcoming paper will extend the investigations to the other polymorphs and examine the conditions for their coexistence. The present paper is organized as follows. In Sec. II we review briefly the state-of-the-art of experiments exploring the magnetic structure of  $\alpha$ -Mn and of previous attempts to calculate the magnetic structure in a collinear approximation. Section III outlines our method, with special reference to the unconstrained vector-field description of the magnetization density. Section IV discusses the calculated crystalline and magnetic structures, Sec. V the electronic structure of  $\alpha$ -Mn, and we summarize in Sec. VI.

## II. CRYSTALLINE AND MAGNETIC STRUCTURE OF $\alpha$ -Mn

### A. State-of-the-art: Experiment

The crystal structure of the nonmagnetic phase of  $\alpha$ -Mn was first resolved by Bradley and Thewlis<sup>3</sup> on the basis of powder x-ray data and shortly later refined by Preston<sup>4</sup> using single-crystal data. The structure is body-centred cubic, space group  $T_d^3-I\bar{4}3m$ , and based on the principle of topological close-packing. The 29 atoms per primitive unit cell (58 atoms per cubic cell) are distributed over four crystallographically inequivalent sites (see Table I). The two atoms occupying sites I are located at the corner and at the center of the cubic cell (see Fig. 1). Atoms of type II are located on tetrahedra centred at sites I, the edge of this tetrahedron measures  $0.515 \times a$  where  $a$  is the lattice parameter of the cubic cell. Sites IV occupy the vertices of a tetrahedron truncated at its four corners such that the small triangular faces decorate the faces of the inner tetrahedron formed by type II atoms (the edge of this larger tetrahedron measures  $0.798 \times a$ ). The 12 MnIV atoms and the 4 MnII atoms together form a CN16 Friauf coordination polyhedron<sup>43</sup> around the

TABLE II. Absolute values of the magnetic moments (in units of  $\mu_B$ ) at the crystallographically inequivalent sites of  $\alpha$ -Mn according to various experiments. In the analysis of the experimental data either a collinear (COLL) or a noncollinear (NCL) structure has been assumed. The number of atoms is per cubic cell

Ref.		Yamagata and Tazawa	Lawson <i>et al.</i>	Yamada <i>et al.</i>	Yamada <i>et al.</i>	Kunitomi <i>et al.</i>	Oberteuffer <i>et al.</i>	Kasper and Roberts	Kasper and Roberts
Model		16	14	13	13	12	11	10	10
Site	No. of atoms	NCL	NCL	NCL A <sup>a</sup>	NCL B <sup>a</sup>	COLL	COLL	COLL A <sup>b</sup>	COLL B <sup>b</sup>
		$\mu_i$	$\mu_i$	$\mu_i$	$\mu_i$	$\mu_i$	$\mu_i$	$\mu_i$	$\mu_i$
I	2	2.05	2.83	2.05	1.9	1.35	1.8	1.54	2.5
II	4 (8)	1.84	1.83	1.79	1.7	1.35	1.4	1.54	2.5
	4	1.75							
IIIa	8 (24)	0.62	0.61	0.61	0.6	0.99	1.2	3.08	1.7
IIIb	16	0.57	0.48	0.57	0.6				
IVa	8 (24)	0.22	0.45	0.22	0.2	0.22	0.1	0.0	0.0
IVb	16	0.31	0.48	0.31					

<sup>a</sup>Models A and B are based on different choices of the magnetic form factor, cf. text.

<sup>b</sup>Models A and B represent different fits to the same set of diffraction data.

MnI atoms. The second-neighbor shell contains the 24 MnIII atoms which form eight equilateral triangles created by truncating a cube (edge  $0.714 \times a$ ) at its eight corners. MnII atoms are also surrounded by a CN16 Friauf polyhedron occupied by 1 MnI, 6 MnIII, and 9 MnIV. MnIII has coordination number (CN) 13 (2 MnII, 7 MnIII, and 4 MnIV). MnIV is icosahedrally surrounded by 1 MnI, 3 MnII, 5 MnIII, and 3 MnIV.

The smallest magnetic unit cell is obtained if antiparallel moments for each pair of atoms at the relative bcc positions  $[(0,0,0) \text{ and } (\frac{1}{2}, \frac{1}{2}, \frac{1}{2})]$  are assumed. Most attempts to determine the magnetic structure are based on magnetic neutron scattering. Shull and Wilkinson<sup>9</sup> first established the existence of antiferromagnetic ordering. Kasper and Roberts<sup>10</sup> demonstrated that the atoms in different sites have different magnetic moments and proposed two different models with nonmagnetic MnIV atoms and large moments varying between  $1.54\mu_B$  and  $3.08\mu_B$  at the remaining sites (see Table II). According to their model, each MnI atom is surrounded by a tetrahedron of MnII atoms with antiparallel moments at a distance of  $2.82 \text{ \AA}$ . Each MnII atom is surrounded by six MnIII at distances of  $2.49$  or  $2.96 \text{ \AA}$  with alternating magnetic moments such that the coupling between neighboring MnIII atoms (distance  $2.67 \text{ \AA}$ ) is antiferromagnetic. On the other hand Arrott *et al.*<sup>44</sup> interpreted the magnetic structure of  $\alpha$ -Mn in terms of a static spin-density wave, in analogy to the magnetic ground-state of antiferromagnetic Cr. A neutron diffraction study by Oberteuffer *et al.*<sup>11</sup> led to qualitative agreement with model B of Kasper and Roberts, albeit with significantly lower values of the magnetic moments (see Table II). Yamada and co-workers<sup>12,13</sup> succeeded in growing a single crystal of  $\alpha$ -Mn and performed a magnetic neutron diffraction study on this sample. As the result of a first analysis, Kunitomi *et al.*<sup>12</sup> proposed a collinear model for the magnetic structure which agrees with Oberteuffer *et al.* on decreasing magnetic moments in the sequence  $|\mu_I| > |\mu_{II}| > |\mu_{III}| > |\mu_{IV}|$ , but predicts even smaller magnetic moments (see Table II). Yamada<sup>45</sup> developed a systematic group-

theoretical approach for determining the magnetic structure of  $\alpha$ -Mn, extending a technique introduced by Bertaut<sup>46</sup> for localized magnetic moments to itinerant systems. A thirteen-parameter model for a noncollinear magnetic structure was proposed. The magnetic point group symmetry is isomorphic to either  $D_{2d}$  or  $C_{3v}$ , depending on the orientation of the principal axis along either  $[100]$  or  $[111]$ . On the basis of the neutron diffraction data, the second alternative could easily be discarded, but the determination of a complete set of parameters depends rather critically on assumptions on the unknown magnetic form factors. Yamada *et al.*<sup>15</sup> constructed altogether five different noncollinear models, all are based on the assumption of a form factor common to all sites. The five form factors are constructed from the Freeman-Watson<sup>48</sup> orbitals of the free Mn atom, using either the  $3d$  orbital alone or admixtures of 10 or 20% of  $4s$  orbitals (which may add or subtract from the  $3d$  form factors). The magnetic moments according to two of these models are listed in Table II. Depending on the choice of the basis functions for the irreducible representations, sites III and IV split into two subgroups each. The absolute values of the magnetic moments are somewhat larger than for the collinear models, but the decrease in the sequence from I to IV is confirmed.

Recently Lawson *et al.*<sup>14</sup> performed high-resolution neutron-diffraction studies on both single-crystal and powder specimens. Their analysis of the experimental data was based on the use of Shubnikov groups, i.e., magnetic space groups that are supergroups of the ordinary crystallographic space groups.<sup>47</sup> The space group of nonmagnetic  $\alpha$ -Mn is  $I\bar{4}3m$  so that the Shubnikov group  $P_1\bar{4}3m$  or one of its subgroups is indicated. The cubic and rhombohedral subgroups were found to be incompatible with the diffraction data, the best fit was obtained with the tetragonal Shubnikov group  $P_1\bar{4}2'm'$ , which is a subgroup of the tetragonal space group  $I\bar{4}2m$ , albeit with an axial ratio of  $c/a = 0.999549$  (hardly deviating from unity), the sites III and IV split into two subgroups each, in accordance with the analysis of Yamada.<sup>45</sup> The

TABLE III. Values of the magnetic moments (in units of  $\mu_B$ ) at the crystallographically inequivalent sites of  $\alpha$ -Mn according to collinear theoretical calculations.

Ref.		Sliwko <i>et al.</i> <sup>a</sup>	Antropov <i>et al.</i> <sup>b</sup>	Asada	Asada	Süss and Krey <sup>a</sup>	Present work <sup>b</sup>	Present work <sup>b</sup>	Present work <sup>c</sup>	Present work <sup>c</sup>
Method		ASW	LMTO-GF	LMTO	LMTO	TB	TB-LMTO	TB-LMTO	VASP	VASP
Functional		LSDA	LSDA	GGA <sup>e</sup>	GGA <sup>f</sup>	Hubbard	LSDA	GGA	GGA <sup>d</sup>	GGA <sup>e</sup>
Site	No. of atoms	$\mu_i$	$\mu_i$	$\mu_i$	$\mu_i$	$\mu_i$	$\mu_i$	$\mu_i$	$\mu_i$	$\mu_i$
I	2	1.79	2.2	2.67	2.82	2.1	3.00	3.26	2.79	3.19
II	8	$\pm 1.43$	-1.8	2.29	2.99	-1.7	-2.31	-2.69	-2.22	-2.79
IIIa	8		0.52				0.66	1.11	1.00	1.81
IIIb	16 (24)	-0.40	-0.52	-0.59	-2.28	0.9	-0.54	-1.10	-1.00	-1.81
IVa	8		-0.17				-0.05	-0.06	0.0	0.00
IVb	16 (24)	-0.17	0.17	0.52	1.72	0.0	0.06	0.07	0.0	0.00

<sup>a</sup>Calculations performed for the cubic structure of paramagnetic  $\alpha$ -Mn.

<sup>b</sup>Calculations performed for the tetragonal structure of antiferromagnetic  $\alpha$ -Mn.

<sup>c</sup>Calculations performed for a fully relaxed tetragonal structure.

<sup>d</sup>Theoretical equilibrium volume (VASP-GGA),  $\Omega = 11.2 \text{ \AA}^3/\text{atom}$ .

<sup>e</sup>Experimental equilibrium volume,  $\Omega = 12.05 \text{ \AA}^3/\text{atom}$ .

<sup>f</sup>Theoretical equilibrium volume (LMTO-ASA),  $\Omega = 13.50 \text{ \AA}^3/\text{atom}$ .

meaning of the Shubnikov-group symbol  $P_1\bar{4}2'm'$  is the same as that of the ordinary space-group symbol  $I\bar{4}2m$ , except that the body-centering operator, the mirror planes, and the twofold rotations are replaced by operators that flip the magnetic moment as the symmetry operation is applied to a magnetic atom. The crystallographic information on the tetragonal structure of the antiferromagnetic phase is summarized in Table I. The magnetic structure is shown to be non-collinear, with a modest canting of the moments on sites II with respect to the direction of those on sites I and a strong canting of the moments on sites IIIa(b) and IVa(b). The absolute values of the magnetic moments are compiled in Table II—for sites I and IV the moments are considerably larger than in the noncollinear model proposed by Yamada *et al.*,<sup>15</sup> comparable moments are predicted for sites III.

The diffraction studies have been supplemented by other experimental investigations. Yamagata and Asayama<sup>16</sup> performed a nuclear magnetic resonance (NMR) study, using the single-crystal specimen on which the diffraction studies of Yamada and co-workers *et al.*<sup>12,13</sup> had been performed. The resonance spectra for the atoms at sites II show two distinct peaks at different hyperfine fields and consequently two types of magnetic moments on sites II, with different magnitudes and different canting angles have been postulated. In view of the group-theoretical analysis of Yamada<sup>45</sup> this means that the magnetic moments of the MnII atoms cannot be described by using a single vector basis function in disagreement with the analysis of the diffraction data. The signal from the site III atoms has a complicated structure. If in analogy to the interpretation of the NMR spectra of the site II atoms, the use of two vector basis functions for representing the magnetic moments of MnIII and MnIV is considered, the consequence is that at both types of sites carry four different types of moments and not only two as derived from the diffraction data. However, the resolution of the

NMR spectra was not sufficient to resolve four different moments. In Table II only the moments corresponding to the two main peaks are listed. The important point is that this work indicates that the magnetic symmetry of  $\alpha$ -Mn might be even lower than derived from the neutron work. However, it is also necessary to emphasize that the analysis is based on the assumption of a cubic crystal symmetry. Given the fact that the cubic symmetry is broken below the Néel temperature, the argument must be reconsidered.

## B. State-of-the-art: Theory

Only a very few attempts have been made to calculate the magnetic ground-state of  $\alpha$ -Mn. Sliwko *et al.*<sup>26</sup> used the local-spin-density approximation (LSDA) and the augmented-spherical-wave (ASW) method<sup>49</sup> to calculate the electronic and magnetic structure for the cubic structure of the paramagnetic phase in a collinear approximation. No structural optimization was performed. The magnitudes of the magnetic moments listed in Table III were found to be in reasonable agreement with those proposed by Yamada *et al.*<sup>15</sup> It is disturbing, however, that according to Sliwko *et al.* out of the four MnII atoms surrounding MnI in a tetrahedral configuration, two have parallel and two antiparallel moments. This contradicts both the structure reported by Yamada *et al.* and the group-theoretical analysis—such a solution cannot be constructed by any linear combination of the vectorial basis functions for site II. That such a solution exists at all indicates a lower symmetry of the magnetic structure. Antropov *et al.*<sup>27</sup> performed calculations using the Greens-function linearized muffin-tin-orbital (LMTO) method, admitting for a tetragonal distortion of the unit cell. Their calculations lead to magnetic moments that are significantly larger than the ASW results (see Table III). This very short paper does not report the actual magnitude of the te-

trigonal distortion, and the absolute values of the moments quoted for the two subsets on sites III and IV are identical and differ only in the sign.

Another LMTO calculation in the atomic sphere approximation (ASA), using the generalized gradient approximation to the exchange-correlation functional was presented by Asada.<sup>28</sup> Asada used the cubic structure determined for the paramagnetic phase, allowing the lattice parameter to relax. The assumed magnetic structure was collinear, with the magnetic moments on the MnIII sites antiparallel to those on the other three types of sites. This assumption is disturbing since it contradicts the results of all experimental analyses. Still, a stable solution with surprisingly large moments could be found (see Table III), which is 79 meV/atom lower in energy than the nonmagnetic solution. Relaxation of the atomic volume leads to an equilibrium lattice constant about 3.6 percent larger than experiment. However, this result must be considered with some caution, given the well-known tendency of the LMTO-ASA to produce too large lattice constants. On expansion, the magnetic moments increase very rapidly, at the equilibrium volume all calculated magnetic moments range between  $1.7\mu_B$  and  $3.0\mu_B$ , i.e., far beyond the experimental estimates, especially for the low-spin MnIII and MnIV sites.

An attempt to determine the noncollinear structure of  $\alpha$ -Mn was made by Süß and Krey.<sup>29</sup> They used a semi-empirical tight-binding method. Their Hamiltonian consists of a paramagnetic part with Slater-Koster parameters for fcc Mn taken from the compilation of Papaconstantopoulos<sup>52</sup> and a Hubbard-type exchange potential, the intra-atomic Coulomb repulsion  $U$  between electrons with parallel spin being treated as an adjustable parameter.  $U \sim 3$  eV was found to be a lower limit for the existence of a well defined antiferromagnetic order—the results for  $U = 3.55$  eV are reported in Table III and found to be in reasonable agreement with the LSDA results. An attempt to determine a noncollinear structure, starting from the model structure by Kunitomi *et al.*<sup>12</sup> failed to produce a convergent result. Nevertheless, this attempt was remarkable because a tendency to split the MnIII and MnIV atoms not only in two, but in three subsets was found. This might indicate that—in accordance with the NMR investigations—the true magnetic structure might have lower symmetry than suggested by the analysis of the neutron diffraction data.

### III. METHODOLOGY

The particular challenge in a calculation of the structural and magnetic ground state of  $\alpha$ -Mn is to achieve simultaneously the high accuracy necessary to determine the structural energy difference between its cubic and tetragonal phases and the magnetic energy differences between different possible spin-structures, and the computational efficiency necessary for treating a system with so many degrees of freedom. Kohn-Sham spin-density functional theory has proved to be a very successful, particularly when used in conjunction with an efficient electronic structure-code.

The tight-binding linear-muffin-tin-orbital technique in the atomic-sphere approximation (TB-LMTO-ASA) (Refs.

50,51) is such a highly efficient tool for calculating the electronic and magnetic structure of even very complex systems. In addition, it permits to treat noncollinear magnetism in a Heisenberg-like approximation, i.e., the spin-quantization axis is fixed within each atomic sphere, but allowed to rotate from one sphere to another.<sup>37,38</sup> However, for delicate problems such as structural and magnetic energy differences, the loss of accuracy due to the ASA may be problematic. Furthermore, interatomic forces cannot be calculated using the LMTO-ASA and hence the technique cannot be used for the optimization of complex crystal structures.

The calculation of the Hellmann-Feynman forces acting on the atoms is straightforward in a plane wave basis. If the electron-ion interactions are described by pseudopotentials, plane-wave techniques are also a very efficient tool for studying the properties of materials at a microscopic level. Standard norm-conserving pseudopotentials are, however, computationally expensive to use, particularly for first-row elements, transition metals, and rare-earth elements. This problem has been circumvented to some extent by the use of ultrasoft pseudopotentials,<sup>30,31,35</sup> which relax the norm-conserving condition that is usually imposed on the pseudo-charge density. This approach has allowed the first-row and transition-metal elements to be treated efficiently. However, substantial difficulties persist for the early 3d-transition metals, where the overlap of the 3d-valence charge density with the 3p “semicore states” cannot be neglected. Difficulties also exist for magnetic transition metals because spin-densities tend to be more localized than charge densities. It has been demonstrated<sup>20</sup> that for the magnetic phases of these materials in particular, the “nonlinear core corrections” introduced by Louie *et al.*<sup>53</sup> to correct for the inherent non-linearity of the exchange-correlation functional are insufficient. Due to the rather localized nature of the spin density, exchange, and correlation must be treated on the basis of the full all-electron charge and spin densities. This is possible using an approach proposed by Blöchl<sup>32</sup> and recently extended by Kresse and Joubert<sup>33</sup> combining ideas from pseudopotentials and linearized-augmented-plane-wave (LAPW) methods into an elegant framework known as the projected augmented wave (PAW) method.

#### A. The projector-augmented-wave method

The PAW method<sup>32,33</sup> is an all-electron method for electronic-structure, total-energy and force calculations which is closely related to the ultrasoft-pseudopotential technique.<sup>30,31</sup> In the PAW approach, charge and spin densities are decomposed into pseudodensities and compensation densities accounting for the difference between the pseudodensities and all-electron densities. The pseudodensities consist of a smooth part expressed in a plane-wave representation and localized augmentation charges accounting for the violation of norm conservation.<sup>30,31</sup> Both augmentation- and compensation charges are represented on radial support grids. Very recently Kresse and Joubert<sup>33</sup> demonstrated that there is a one-to-one correspondence between ultrasoft pseudopotentials and the PAW approach and adapted the technique to metallic systems. The advantage of

the PAW technique is that it is an all-electron approach and provides the full wave functions that are not directly accessible with the pseudopotential approach. Additionally, the potential is determined from the full charge density.

The all-electron wave function  $|\Psi_m\rangle$  is generated from the pseudo wave function  $|\tilde{\Psi}_m\rangle$  using

$$|\Psi_m\rangle = |\tilde{\Psi}_m\rangle + \sum_i (|\phi_i\rangle - |\tilde{\phi}_i\rangle) \langle \tilde{p}_i | \tilde{\Psi}_m \rangle. \quad (1)$$

The all-electron partial waves  $|\phi_i\rangle$  are obtained by radially integrating the Schrödinger equation for a set of energies  $\epsilon_k$  and are orthogonalized to the core states. Here the index  $i$  is a short-hand notation for the atomic site  $\mathbf{R}_i$ , the valence-electron quantum numbers  $nlms$  and the reference energies  $\epsilon_k$  used for the construction of the projectors. The index  $m$  stands for the band-index and the  $\mathbf{k}$  points within the first Brillouin zone.  $|\tilde{\phi}_i\rangle$  are the pseudo partial waves, which are functions of a radial grid multiplied by spherical harmonics, and coincide with the corresponding all-electron partial waves outside some augmentation region. Finally, the projector function  $|\tilde{p}_i\rangle$  for each pseudo partial wave is localized within the augmentation region and obeys the relation  $\langle \tilde{p}_i | \tilde{\phi}_j \rangle = \delta_{ij}$ . In this formalism, the charge density at a point  $\mathbf{r}$  is the expectation of the real-space projection operator  $|\mathbf{r}\rangle\langle\mathbf{r}|$  and is given by

$$n(\mathbf{r}) = \tilde{n}(\mathbf{r}) + n^1(\mathbf{r}) - \tilde{n}^1(\mathbf{r}), \quad (2)$$

where the soft pseudocharge density is

$$\tilde{n}(\mathbf{r}) = \sum_m f_m \langle \tilde{\Psi}_m | \mathbf{r} \rangle \langle \mathbf{r} | \tilde{\Psi}_m \rangle \quad (3)$$

( $f_m$  stands for the Fermi-Dirac occupation function). The on-site charge-densities,  $n^1$  and  $\tilde{n}^1$ , are expressed in terms of the projector functions and the pseudowaves- and all-electron partial waves,

$$n^1(\mathbf{r}) = \sum_{m,(i,j)} f_m \langle \tilde{\Psi}_m | \tilde{p}_i \rangle \langle \phi_i | \mathbf{r} \rangle \langle \mathbf{r} | \phi_j \rangle \langle \tilde{p}_j | \tilde{\Psi}_m \rangle \quad (4)$$

and

$$\tilde{n}^1(\mathbf{r}) = \sum_{m,(i,j)} f_m \langle \tilde{\Psi}_m | \tilde{p}_i \rangle \langle \tilde{\phi}_i | \mathbf{r} \rangle \langle \mathbf{r} | \tilde{\phi}_j \rangle \langle \tilde{p}_j | \tilde{\Psi}_m \rangle. \quad (5)$$

The total energy can be expressed as

$$E = \tilde{E}[\tilde{n}(\vec{r})] + E^1[n^1(\vec{r})] - \tilde{E}^1[\tilde{n}^1(\vec{r})], \quad (6)$$

where  $\tilde{E}$ ,  $E^1$ , and  $\tilde{E}^1$  are functionals of the wavefunctions and the charge densities listed above. We refer the interested reader to the paper of Kresse and Joubert<sup>33</sup> for further theoretical details. The particular advantage of the PAW technique is that it combines the accuracy of the best all-electron methods with the efficiency of the most advanced pseudopotential techniques.

For magnetic calculations, orbitals and charge densities must be calculated separately for spin-up and spin-down

electrons. A total charge-density and a spin-density may be calculated by taking the sum and the difference of the spin-up and spin-down densities, respectively. As long as only collinear magnetic structures with a fixed spin-quantization axis are considered, charge and spin densities are scalar quantities and the step from nonspin-polarized to spin-polarized calculations is trivial. The situation is much more complex for noncollinear magnetic structures.

## B. LSDA and GGA for noncollinear spin structures

Von Barth and Hedin's<sup>54</sup> local-spin-density theory implicitly allows for noncollinear spin arrangements, but Kübler *et al.*<sup>37,55</sup> and Sandratskii and Guletskii<sup>56</sup> were the first to implement the noncollinear description in an electronic-structure code. Following Kübler *et al.*,<sup>37,55</sup> the total energy is expressed in terms of a  $2 \times 2$  density matrix with elements  $n_{\text{Tr}}(\mathbf{r}) = n^{\alpha\beta}(\mathbf{r})$ , where  $\alpha, \beta = \uparrow, \downarrow$  stand for the spin quantum numbers. The electron density is then given by the trace  $\text{Tr}[n^{\alpha\beta}(\mathbf{r})]$  of the density matrix. The vectorial magnetization density is defined by the projection of the density matrix on the vector of the Pauli spin matrices  $\vec{m}(\mathbf{r}) = \sum_{\alpha\beta} n^{\alpha\beta}(\mathbf{r}) \cdot \vec{\sigma}^{\alpha\beta}$ . In the Kohn-Sham density functional the kinetic-energy contribution is calculated in terms of the spin-up and spin-down eigenfunctions, the electrostatic terms depend on the scalar density  $n_{\text{Tr}}$  only. In the local-spin-density approximation the exchange-correlation energy  $E_{\text{xc}}[n^{\alpha\beta}]$  is defined by

$$\begin{aligned} E_{\text{xc}}[n^{\alpha\beta}] &= \int n_{\text{Tr}}(\mathbf{r}) \epsilon_{\text{xc}}[n^{\alpha\beta}(\mathbf{r})] d\mathbf{r} \\ &= \int n_{\text{Tr}}(\mathbf{r}) \epsilon_{\text{xc}}[n_{\text{Tr}}(\mathbf{r}), |\vec{m}(\mathbf{r})|] d\mathbf{r}. \end{aligned} \quad (7)$$

The density matrix  $n^{\alpha\beta}(\vec{r})$  is composed of a soft pseudodensity and augmentation and compensation contributions—in complete analogy to the scalar case. The generalization is straightforward—it is sufficient to add spin-indices to the pseudo wave function  $\langle \tilde{\Psi}_m | \mathbf{r} \rangle \rightarrow \langle \tilde{\Psi}_m^\alpha | \mathbf{r} \rangle$ . The actual functional form of  $\epsilon_{\text{xc}}$  can be parametrized in several ways. In the LSDA, we used the exchange-correlation functional proposed by Perdew and Zunger<sup>57</sup> based on the quantum Monte Carlo simulations of Ceperley and Alder<sup>58</sup> for the interacting electron gas. For the intermediate spin polarizations we used the interpolation proposed by von Barth and Hedin.<sup>54</sup>

The generalized gradient approximation (GGA) has been developed with the aim of incorporating the leading nonlocal corrections to the LDA. In the GGA, the terms added to the exchange-correlation functional depend also on the gradients of electron-density and magnetization spin density and because in a noncollinear description, there is no global spin-quantization axis, this leads to further approximations. Even if there is no global magnetization axis, at every point in space a local coordinate system may be defined such that the magnetization points along the local  $z$  axis. In evaluating the GGA contributions to the exchange-correlation functional, for the evaluation of the gradients only projections of the

magnetization on the local spin-quantization axis are used in a standard GGA. This approximate treatment should be accurate if the magnetization direction rotates only slowly.

Out of the many different GGA functionals proposed in the literature we choose the form proposed by Perdew *et al.*,<sup>59</sup> the approach of White and Bird<sup>60</sup> has been used to calculate the spin-polarized GGA potentials.

### C. Local spin-quantization axes vs unconstrained vector-field description of magnetization

The actual implementation of the noncollinear LSDA depends considerably on the band-structure method. Within the ASW, (TB-)LMTO, and TB techniques, a spin-quantization axis is assigned to each atomic site and the local spin-up and spin-down orbitals are related to global spin-coordinates by a rotation in spin space.<sup>37,38,56,55</sup> The direction of the magnetic moments changes discontinuously from one site to the next—evidently this picture is most appropriate for local-moment magnetism. The implementation within the PAW and full-potential linearized augmented-plane-wave (FLAPW) approaches is much better adapted for itinerant magnetic systems: The plane-wave part of the magnetization density (and the corresponding contributions to orbitals and potentials) is represented by a vector field on a regular three-dimensional grid in real and reciprocal space. In the PAW approach this grid covers the complete cell, in the FLAPW approach the plane-wave description applies only to the interstitial space outside the muffin-tin spheres. The augmentation and compensation charges of the PAW, and the charges inside the muffin-tin spheres in the FLAPW approach are represented on spherical support grids.<sup>41,42,40</sup> If only the spherical-symmetric part is included, this corresponds to assigning a fixed spin-quantization axis to the augmentation and compensation charges and the muffin-tin spheres, respectively. In this approximation, intra-atomic magnetic noncollinearity is excluded in the FLAPW, whereas in the PAW it is admitted as far as it is describable by the plane-wave contributions alone. If contributions to the on-site terms from higher-order spherical harmonics are admitted, a full description of intra-atomic noncollinearity is achieved.<sup>41,42</sup> Intra-atomic noncollinearity has been found to be of decisive importance in determining the correct spin-wave ground state of  $\gamma$ -Fe (Refs. 61,62) and is also known to exist in magnetic lanthanides and actinides where spin-orbit coupling is important.<sup>41</sup> The unconstrained vector-field description is particularly valuable when the GGA is used as jumps in the magnetization directions are avoided. As magnetization is described by a continuously varying vector field, local magnetic moments associated with individual atoms can be calculated only by integrating the magnetization density over an atomic cell or atomic sphere. It must be born in mind that these magnetic moments are only local projections. For any details of the implementation on noncollinear magnetism in the PAW we refer to our recent work.<sup>42</sup>

### D. Computational setup

Our calculations have used the Vienna LMTO package and the Vienna *ab initio* simulation package VASP.<sup>33,63,64</sup> The

Vienna LMTO package<sup>65</sup> is a standard semirelativistic linearized muffin-tin orbital code using the atomic sphere approximation and the so-called combined correction terms.<sup>50,51</sup> In the TB-LMTO the most localized basis set is constructed via a canonical transformation. The atomic sphere radius is the same on all types of Mn sites. Noncollinear spin structures may be treated in an approximation assigning individual spin-quantization axes to the atomic spheres.<sup>38</sup>

VASP is a first-principles plane-wave code which treats exchange and correlation in the local density approximation potentials<sup>30,31</sup> or using projector-augmented waves.<sup>32,33</sup> Here the all-electron PAW method has been used. The solution of the Kohn-Sham equations is performed using an efficient iterative matrix diagonalization routine based on a sequential band-by-band residual minimization method—direct inversion in the iterative subspace (RMM-DIIS) is used. The charge density is updated using an improved Pulay mixing.<sup>66</sup> For the spin-polarized exchange and correlation potentials the GGA functional of Perdew *et al.*<sup>59</sup> as implemented by White and Bird<sup>60</sup> is employed. The same GGA functional has also been used for the construction of the PAW potentials.

The optimization of the atomic geometry, including ionic coordinates, volume and shape of the unit cell, is performed via the conjugate-gradient minimization of the total energy, using the Hellmann-Feynman forces on the atoms and stresses on the unit cell. Brillouin zone integrations in our calculations are performed on a grid of Monkhorst-Pack special points<sup>67</sup> using grids varying from  $2 \times 2 \times 2$  to  $8 \times 8 \times 8$  depending on the size of the unit cell (this refers to calculations for the other polymorphs with simpler crystal structures). The Methfessel-Paxton scheme with a broadening of 0.1 eV has been used for calculating density-of-states and is rapidly convergent with respect to the  $k$ -point grid. For the noncollinear spin structures of the  $\alpha$  phase, the calculations had to be restricted to the coarsest grid. As the calculations have been performed within symmetry constraints, the full Brillouin zone has to be sampled. Hence even a  $2 \times 2 \times 2$  mesh corresponds to a grid of 64  $k$  points. However, the calculations for the collinear configurations performed on a finer grid allow us to conclude that convergence beyond the level of the energy differences between the collinear and noncollinear phases has been achieved even with this coarse grid. For a final analysis of the electronic density of states, finer meshes and a tetrahedron-integration technique have been used. The cutoff energy for the plane wave expansion was fixed at 250 eV for  $\alpha$ -Mn, although larger cutoffs of 275 eV are used for phases with smaller unit cells for testing purposes.

The noncollinear calculations were performed using the fully unconstrained approach recently developed within our group<sup>42</sup> and briefly sketched above. The method allows both the atomic and magnetic structures to relax simultaneously and self-consistently and the magnetization density is described as a continuous vector variable of position. Noncollinear solutions have been attempted using both the collinear magnetic structure and the magnetic moments chosen to reflect the experimental data of Yamada *et al.*<sup>15</sup> as a starting point.

An important point to be emphasized is that the structural relaxation (both atomic and magnetic) has been performed without any symmetry constraint. This is in contrast to most *ab initio* crystallographic optimization which are performed under the constraint of conservation of the space-group symmetry and where charge densities, potentials, and forces are symmetrized after each iteration. For  $\alpha$ -Mn the discussion in Sec. II has shown that the magnetic symmetry of the noncollinear spin arrangement is not uniquely determined by experiment. To solve this open question, we proceed to an unconstrained structural optimization. The drawback is that without explicit symmetrization of charge and spin densities and of the interatomic forces and magnetic torques, a higher level of convergence must be achieved to avoid spurious symmetry breaking due to numerical fluctuations. The very small deviation of the axial ratio of the tetragonal antiferromagnetic phase from unity illustrates that a very high accuracy is indeed required. For the present calculations, convergence criteria have been set for the electronic and magnetic relaxations to changes in the total energy per atom smaller than  $10^{-5}$  eV, for the structural relaxations at fixed cell volumes, forces had to be converged to at least 0.1 eV/Å.

#### IV. CRYSTALLINE AND MAGNETIC STRUCTURE OF $\alpha$ -Mn

##### A. Magnetic structure using the TB-LMTO-ASA method

Calculations of the electronic and magnetic structure of  $\alpha$ -Mn in the tetragonal crystal structure of Lawson *et al.*<sup>14</sup> and using the experimentally determined lattice constants and structural parameters have been performed using the LMTO-ASA method in both the LSDA and the generalized gradient approximation (GGA) to the exchange-correlation functional. Brillouin-zone integrations have been performed using  $2 \times 2 \times 2$  and  $3 \times 3 \times 3$   $k$ -point grids (the latter corresponding to 14  $k$ -points in the irreducible Brillouin zone) and Methfessel-Paxton smearing. A comparison of the results shows that for calculating total energies the coarser grid is largely sufficient. A first set of calculations was performed in a collinear approximation. As previous LMTO and ASW calculations<sup>26–28</sup> disagree even on the sign of the coupled of the magnetic moments on the inequivalent Mn sites, different initializations of the magnetic structure have been chosen: (a) magnetic moments on the MnI and MnII sites only and (b) nonzero magnetic moments on the MnIII and MnIV sites as well. Both sets of calculations converged exactly to the same solution, with antiparallel orientation of the MnI and MnII moments, in accordance with all experimental estimates.

We find significant differences compared to previous LSDA calculations.<sup>26,27</sup> In comparison to Sliwko *et al.*, the much larger moments predicted for sites I and II (see Table II) are certainly the consequence of their assumption of a ferromagnetic coupling of the MnI atoms to two of its four MnII neighbors. The purely antiferromagnetic MnI-MnII coupling resulting from our calculation allows the formation of larger local MnI and MnII moments. Our magnetic moments on sites MnI and MnII are also larger than those calculated by Antropov *et al.* Unfortunately, no details of the

calculations are given in the paper of Antropov *et al.*<sup>27</sup> (the paragraph on  $\alpha$ -Mn is just ten lines), so we can only speculate that there is a correlation between the smaller moments on sites MnI and MnII, and the larger moments on sites MnIII and MnIV.

The larger moments on sites MnI and MnII agree with the GGA results of Asada,<sup>28</sup> the differences in the MnIV moments are probably due to the difference in the basic assumptions concerning the relative orientation of the MnI and MnII moments (remember that each MnI atom is surrounded by four MnII and 12 MnIV). The broken cubic symmetry is reflected by small differences in the moments on sites III-(IV)a and III(IV)b (but see the discussion of the noncollinear structure below). The GGA tends to enhance the large moments on sites I to III, but hardly affects those on sites IV. This indicates that the almost vanishing moments on sites MnIV are the consequence of a geometrical frustration. Using a Greens-function tight-binding (TB) LMTO technique, we have analyzed the distance dependence of the exchange-pair-interactions in a Heisenberg-like model. Strongly negative (antiferromagnetic) coupling was found at short interatomic distances, switching to positive coupling at larger distances. Around the MnI site for example, the exchange interaction with the 4MnII and 12 MnIV neighbors on the CN16 coordination polyhedron is strongly antiferromagnetic, whereas the coupling to the 24 MnIII neighbors on the second coordination shell is essentially zero. Pair interactions over larger distances are ferromagnetic. This analysis confirms the relative orientation of the MnI and MnIV moments and also provides a rationale for the strong quenching of the MnIV moments. Using the version of the LMTO technique allowing for different spin-quantization axes in inequivalent atomic spheres, we have also attempted to find a noncollinear solution, but spin structures initialized according to the models proposed in the literature always relaxed back to the collinear solution.

##### B. Crystalline and magnetic structure using PAW

We begin by discussing the relative stability of the nonmagnetic, collinear antiferromagnetic and noncollinear antiferromagnetic phases of  $\alpha$ -Mn. For all magnetic phases the crystalline structure has been optimized independently. Figure 2(a) shows the total energy of paramagnetic and both collinear and noncollinear antiferromagnetic  $\alpha$ -Mn as a function of volume and Fig. 2(b) shows the variation of the magnitude of the magnetic moments on the crystallographically inequivalent sites. The magnetic structure is found to be strongly coupled to the crystal structure—Fig. 3 reports the calculated variation of the axial ratio and of the internal atomic coordinates of all three magnetic phases as a function of volume. The onset of magnetic ordering occurs at an atomic volume of about  $9.5 \text{ \AA}^3$ , up to a volume of about  $12 \text{ \AA}^3$  the magnetic structure remains collinear, with nonmagnetic Mn atoms on sites IV. For larger atomic volumes, a metastable collinear magnetic configuration coexists with the stable noncollinear phase.

To find this noncollinear structure turned out to be extremely difficult: initially all calculations performed close to

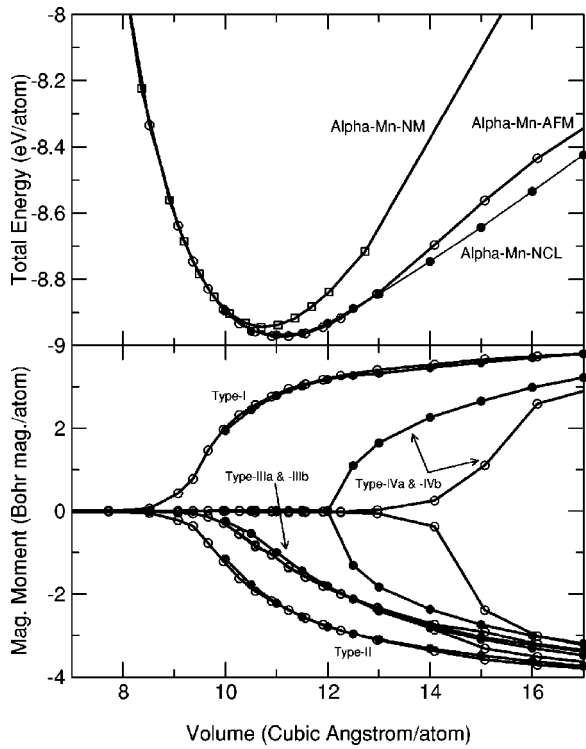


FIG. 2. (a) Total energy of nonmagnetic (NM), collinear antiferromagnetic (AFM) and noncollinear antiferromagnetic (NCL)  $\alpha$ -Mn as a function of volume. (b) Absolute values of the calculated magnetic moments on the crystallographically inequivalent sites in noncollinear antiferromagnetic  $\alpha$ -Mn. The nomenclature is as given in Table I. Sites III and IV split into two subsets in the tetragonally distorted antiferromagnetic phase.

the experimental density (in the volume range of 10 to 13  $\text{\AA}^3$ ) converged to a collinear solution, even if the starting point for the optimization of the noncollinear spin arrangement was chosen close to one of the noncollinear structures proposed in the literature. Finally we decided as the last attempt to optimize the magnetic structure at a strongly expanded volume of 16  $\text{\AA}^3$ , starting with the noncollinear magnetic structure proposed by Lawson *et al.*<sup>14</sup> but with artificially enhanced magnetic moments on the MnIV sites which showed a pronounced volume dependence at higher densities. This calculation converged to a well defined noncollinear minimum substantially lower in energy than the still metastable collinear structure. Noncollinear solutions at lower volumes could than be found by using a rescaled atomic and magnetic structure as the starting point for the optimization at stepwise increased density. The volume dependence of the site-dependent magnetic moments and of the internal coordinates explains this surprising result: As long as the MnIV atoms are nonmagnetic, the collinear antiferromagnetic structure is only weakly frustrated. The coupling between MnI and MnII is antiferromagnetic, the frustration of the magnetic coupling in the triangular groups of MnIII (MnIIIa and MnIIIb atoms couple antiferromagnetically) atoms is released by distorting the equilateral triangles to isosceles triangles. Beyond a critical volume, magnetic moments on the MnIV develop. In a collinear spin structure, the MnIV

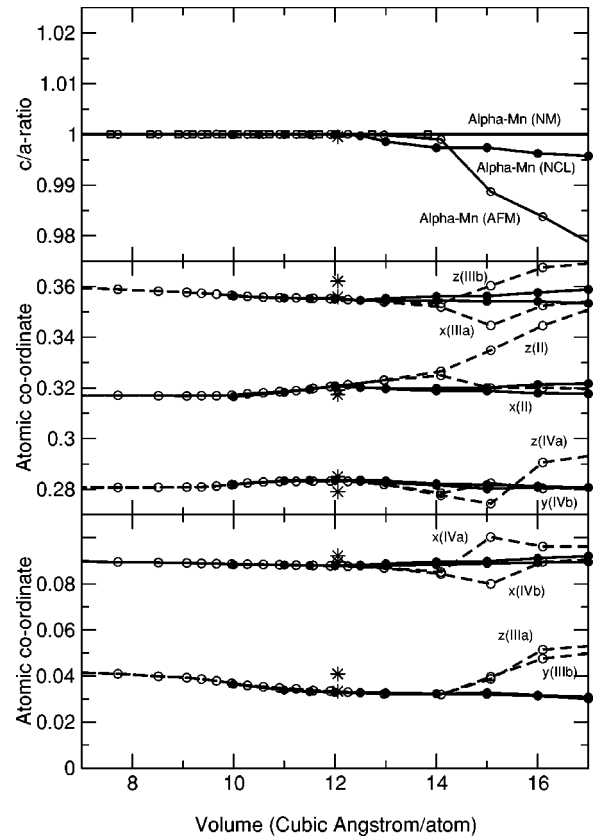


FIG. 3. Variation of the axial ratio  $c/a$  (upper panel) and of the internal structural parameters (for the notation see Table I) of antiferromagnetic  $\alpha$ -Mn as a function of volume. The empty circles mark the results calculated for the collinear phase, the full circle the results for a noncollinear magnetic structure, open squares the results for the non-magnetic phase. Full and broken lines are a guide to the eye. The asterisks mark the experimental data of Lawson *et al.* (Ref. 14).

moments increase only very slowly, the magnetic frustration is reduced by a rather pronounced distortion of the crystal structure which is much stronger than experimentally observed. If a canting of the magnetic moments from their collinear directions is admitted, the MnIV moments increase very rapidly, showing almost critical behavior. As the frustration of the magnetic exchange interactions is strongly reduced by the spin canting, the distortion of the crystalline structure is much weaker. In the following we discuss the magnetic and crystalline structure of all three phases in more detail.

### C. Paramagnetic $\alpha$ -Mn

In the paramagnetic phase, the cubic A12 structure is found to represent the ground state. The optimized internal structural parameters are found to be in very good agreement with experiment (see Table I), but the calculated lattice constant and equilibrium volume ( $a = 8.532 \text{ \AA}$ ,  $\Omega = 10.71 \text{ \AA}^3$ ) are substantially lower than the experimental data for the paramagnetic phase extrapolated to zero temperature ( $a = 8.86 \text{ \AA}$ ,  $\Omega = 11.99 \text{ \AA}^3$ ). An error of 3.7% in a lattice constant and of 10.6% in the atomic volume calculated in the

GGA has to be considered as an unusually large error for a 3d metal, but one has to emphasize that the extrapolation of the experimental lattice constants introduces some uncertainty.

#### D. Collinear antiferromagnetic $\alpha$ -Mn

The calculated equilibrium volume of antiferromagnetic  $\alpha$ -Mn is  $\Omega = 11.23 \text{ \AA}^3$ , compared to an experimental volume of  $\Omega = 12.05 \text{ \AA}^3$  according to Lawson *et al.*,<sup>14</sup> i.e., the error in the atomic volume is reduced to 6.8%. For comparison: For antiferromagnetic bcc Cr, the most accurate GGA calculations also underestimate the atomic volume by 4.1%.<sup>22,68</sup> For antiferromagnetic  $\gamma$ -Fe, GGA calculations also lead to a predicted equilibrium volume that is about 7% smaller than the atomic volume of  $\gamma$ -Fe precipitates in a Cu matrix.<sup>62</sup> For the ferromagnetic metals Fe, Co, and Ni on the other hand, the GGA predicts lattice constants in almost perfect agreement with experiment.<sup>20</sup> Hence it appears that the GGA is less successful in correcting the LSDA overbinding for antiferromagnetic than for ferromagnetic 3d metals.

At this volume the magnetic structure is essentially still collinear, although the cubic crystal symmetry is broken. The axial ratio is still very close to unity, but the internal parameters summarized in Table I show that some of the relations holding only in the cubic limit [ $x(\text{II})=z(\text{II})$ ,  $x(\text{IIIa})=z(\text{IIIb})$ ,  $x(\text{IVa})=x(\text{IVb})$ ,  $y(\text{IIIb})=z(\text{IIIa})$ ] are already slightly violated. Compared to earlier collinear calculations, the high magnetic moments on sites I and II predicted by our LMTO calculations are confirmed, but the full-potential PAW calculations lead to larger MnIII and even smaller MnIV moments than the LMTO calculations performed in an atomic-sphere approximation, see Table III. The onset of a formation of a magnetic moment on the MnIV sites takes place only close to the experimental volume. There are considerable differences compared to some of the previous collinear calculations: In agreement with Antropov *et al.*<sup>27</sup> and Süß and Krey<sup>29</sup> and with our own TB-LMTO calculations, but in disagreement with Sliwko *et al.*<sup>26</sup> and with Asada<sup>28</sup> we find that the MnI atom couples antiferromagnetically to all four MnII atoms surrounding the central atom—Sliwko *et al.* had reported ferromagnetic and antiferromagnetic coupling to groups of two MnII atoms sharing a common edge of the MnII tetrahedron, Asada had assumed a ferromagnetic interaction. We note that if the MnII atoms were divided into two magnetically inequivalent groups, this would result in a further lowering of the magnetic symmetry which is incompatible with the symmetry analysis of Yamada.<sup>45</sup> Furthermore, in the models of Sliwko *et al.* and of Asada, all MnIII atoms carry parallel moments so that no frustration would occur in the triangular MnIII groups. We find, again in agreement with Antropov *et al.* that the four MnIIIa atoms couple ferromagnetically to the central MnI moment, whereas the eight MnIIIb atoms couple antiferromagnetically. Hence on an equilateral MnIII triangle there are one positive and two negative moments and at least one of the exchange interactions is necessarily frustrated and this drives the structural distortion. There are also important differences concerning the MnIV moments: Our TB-LMTO and PAW calculations

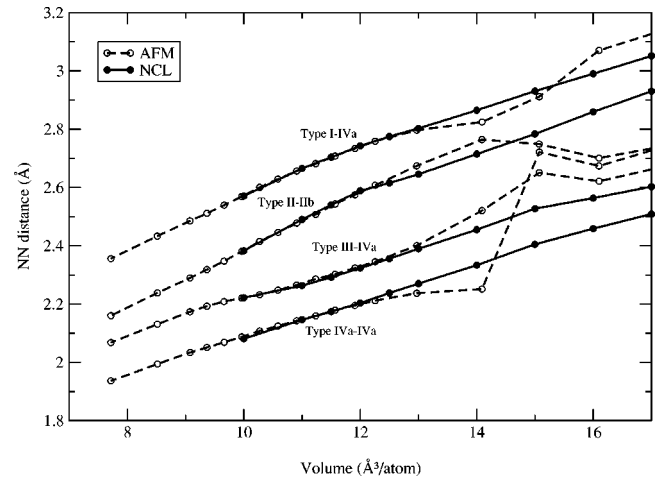


FIG. 4. Variation of selected interatomic distances in  $\alpha$ -Mn with volume: open symbols and broken lines: collinear antiferromagnetic phase, full symbols and full lines: noncollinear phase.

agree on almost vanishing magnetic moments on these sites, in agreement with Süß and Krey.<sup>29</sup> Sliwko *et al.*<sup>26</sup> and Antropov *et al.*<sup>27</sup> report slightly larger moments which are, however, still appreciably lower than the MnIII moments whereas in Asada's results MnIII and MnIV moments are nearly equal at the experimental density.

At expanded volume, as a substantial moment on the MnIV sites develops, collinear antiferromagnetic Mn undergoes a strong structural distortion—much stronger than observed experimentally. This concerns the shape of the unit cell as well as the internal atomic positions (see Fig. 3). The variation of the internal parameters leads to strong changes in the interatomic distances—the variation of a few characteristic distances is shown in Fig. 4. We find that in particular the short distances between magnetically equivalent MnIV atoms increase strongly—at larger distances the antiferromagnetic interaction decreases strongly and hence the strong distortion of the MnIV triangle helps to reduce the magnetic frustration.

#### E. Noncollinear antiferromagnetic $\alpha$ -Mn

A noncollinear magnetic structure develops only at a volume slightly larger than equilibrium. While the magnetic moments at sites I to III continue to increase slowly (and hardly differ from their values in the collinear phase at all), in the noncollinear phase the magnetic moment on the MnIV sites shows critical behavior beyond  $\Omega \sim 12 \text{ \AA}^3$ . The formation of MnIV moments triggers the noncollinear canting of the magnetic moments. This is illustrated in Fig. 5 showing a three-dimensional representation of the magnetic structure at different atomic volumes. While the moments on sites I and II remain always collinear, those on sites III remain in a collinear orientation only as long as the MnIV moments are zero. The MnIV atoms are arranged on the small triangular faces of a truncated tetrahedron, the interatomic distances in these small triangles are the shortest in  $\alpha$ -Mn. At these short interatomic distances, the exchange interaction between Mn

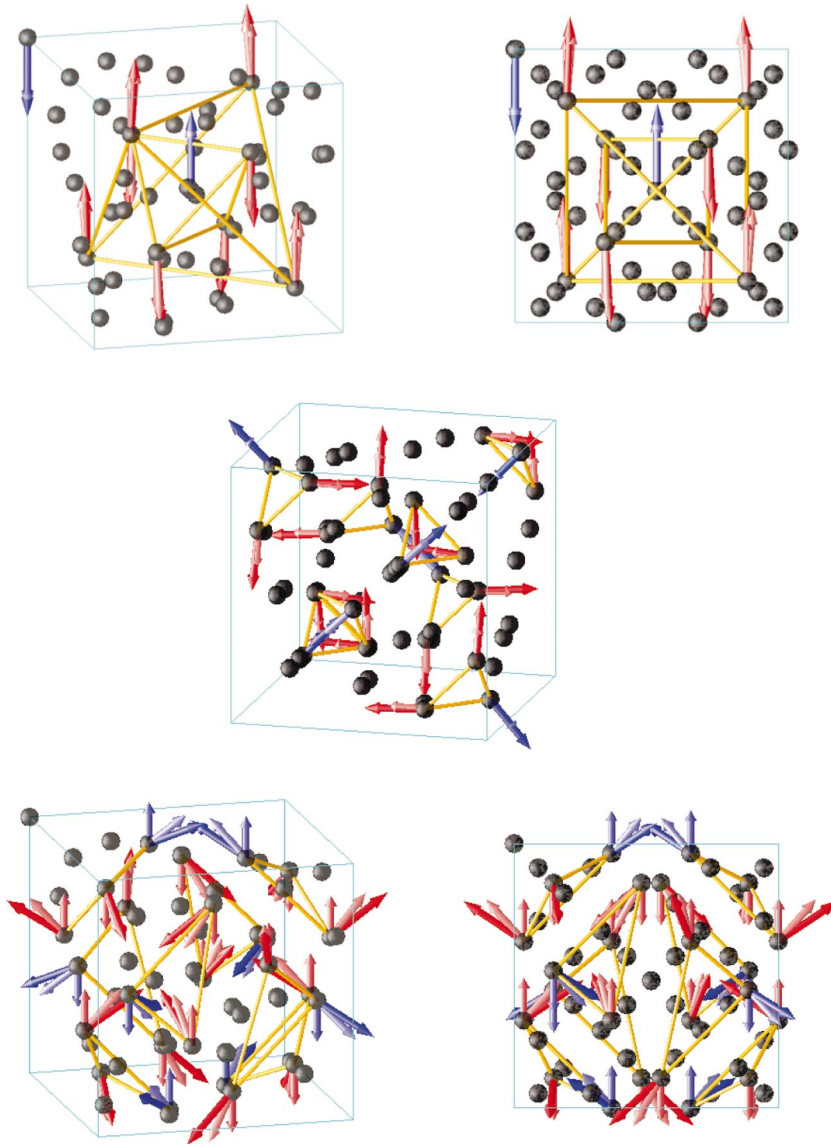


FIG. 5. (Color) Noncollinear magnetic structure of  $\alpha$ -Mn. Top row: Magnetic moments on sites I (blue arrows) and sites II (purple arrows), viewed slightly of top (left) and from the front (right). Arrows of different length and shading indicate the increase of the magnetic moments on expansion from  $\Omega = 12$  to  $14 \text{ \AA}^3$ . Central panel: Magnetic moments on the type-IV atoms (blue: IVa, purple: IVb), viewed slightly off-front. The yellow bars mark the short interatomic distances between atoms forming the small triangular faces of a truncated tetrahedron. Note that the moments on each of these MnIV trimers forms a spin structure with angle of about  $120^\circ$  between neighboring moments similar to the Néel phase of a frustrated triangular antiferromagnet. Bottom row: Magnetic moments on sites III (blue: IIIa, purple: IIIb). Note how with increasing volume and increasing magnetic moment on the MnIV sites the MnIII moments rotate away from the direction collinear to the moments on sites I and II. At  $\Omega = 12 \text{ \AA}^3$ , the collinear arrangement is still marginally stable.

atoms is always strongly antiferromagnetic as shown by the The Greens-function LMTO calculations. Hence the situation is similar to that in a frustrated triangular antiferromagnet, and indeed we find that the three MnIV atoms (1 MnIVa and 2 MnIVb) on a triangle are oriented roughly at  $120^\circ$  relative to each other, similar to the Néel structure which forms the ground-state of a triangular antiferromagnet within the XY model (in reality, the moments deviate slightly from a planar arrangement and differ slightly in magnitude). Once the MnIV atoms are magnetically polarized, the MnIII moments begin to rotate away from their orientation collinear to the MnI and MnII moments, the canting increasing parallel

to the MnIV moments. Whereas the MnIII moments undergo a large rotation as the volume and the magnetic moments increase, the directions of the MnIV moments do not change at all. This demonstrates that the driving force for the formation of a noncollinear structure is really the frustration of the antiferromagnetic coupling in the MnIV triangles. Again the increase of the moments on sites III and IV is accompanied by a structural distortion—but this distortion is now much more modest than that calculated for the collinear phase and in good agreement with experiment (almost within the combined experimental and computational uncertainty). As shown in Fig. 4 all interatomic distances scale similarly with

TABLE IV. The internal structural parameters and magnetic moments ( $\mu_B$ ) for  $\alpha$ -Mn at a series of volumes, compared with the experimental data. The convention adopted for the Cartesian components of the magnetic moments is the following: Moments on sites I are aligned along [001]. The moments for sites III and IV are listed for a set of three atoms forming a common triangle—these are always atoms from all three different subgroups (a,b1,b2). In the collinear limit the moments on sites a and B are antiparallel.

		Experiment (Ref. 14)								
		I	II	IIIa	IIIb	IVa	IVb			
$V = 12.05 \text{ \AA}^3$	$x$	0.0	0.319	0.362	0.353	0.092	0.089			
	$y$	0.0	0.319	0.362	0.033	0.092	0.285			
	$z$	0.0	0.317	0.041	0.356	0.279	0.089			
	$M_x$	0.0	0.14	0.43	-0.25	0.27	-0.08			
	$M_y$	0.0	0.14	0.43	-0.25	0.27	-0.45			
	$M_z$	2.83	-1.82	0.43	-0.32	-0.45	0.48			
	$ M $	2.83	1.83	0.74	0.48	0.59	0.66			
		Theory (Present work)								
		I	II	IIIa	IIIb1	IIIb2	IVa	IVb1	IVb2	
$V = 12 \text{ \AA}^3$	$x$	0.0	0.320	0.355	0.355		0.088	0.088		
	$y$	0.0	0.320	0.355	0.033		0.284	0.284		
	$z$	0.0	0.320	0.033	0.355		0.283	0.088		
	$M_x$	0.0	-0.01	0.01	0.0	-0.03	0.0	0.0	0.0	
	$M_y$	0.0	-0.01	0.02	0.0	-0.01	0.0	0.0	0.0	
	$M_z$	3.19	-2.79	1.81	-1.81	-1.81	0.0	-0.01	-0.02	
	$ M $	3.19	2.79	1.81	1.81	1.81	0.0	0.01	0.02	
$V = 13 \text{ \AA}^3$	$x$	0.0	0.320	0.355	0.355		0.088	0.088		
	$y$	0.0	0.320	0.355	0.033		0.088	0.283		
	$z$	0.0	0.319	0.032	0.354		0.283	0.087		
	$M_x$	0.0	0.24	-1.24	0.53	-1.58	1.25	0.09	-1.64	
	$M_y$	0.0	0.24	-1.37	-1.18	0.20	1.32	-1.64	0.01	
	$M_z$	3.33	-3.09	1.49	-2.03	-1.76	0.14	0.03	0.02	
	$ M $	3.33	3.10	2.37	2.41	2.37	1.83	1.64	1.64	
$V = 14 \text{ \AA}^3$	$x$	0.0	0.320	0.356	0.355		0.088	0.090		
	$y$	0.0	0.319	0.355	0.032		0.089	0.282		
	$z$	0.0	0.319	0.032	0.354		0.282	0.087		
	$M_x$	0.01	-0.31	-1.64	0.82	-2.16	1.61	0.18	-2.26	
	$M_y$	0.02	-0.01	-1.76	-1.78	0.40	1.73	-2.26	0.06	
	$M_z$	3.47	-3.30	-0.32	-2.03	-1.74	0.22	0.04	0.05	
	$ M $	3.47	3.31	2.74	2.82	2.80	2.37	2.26	2.26	
$V = 15 \text{ \AA}^3$	$x$	0.0	0.320	0.356	0.355		0.089	0.090		
	$y$	0.0	0.320	0.356	0.032		0.089	0.282		
	$z$	0.0	0.319	0.033	0.354		0.280	0.086		
	$M_x$	-0.01	-0.19	-1.90	0.81	-2.56	1.86	0.26	-2.66	
	$M_y$	0.0	0.12	-2.01	-2.22	0.21	2.00	-2.65	0.12	
	$M_z$	3.59	-3.48	1.27	-2.00	-1.71	0.29	0.04	0.06	
	$ M $	3.59	3.49	3.05	3.10	3.08	2.74	2.66	2.66	

increasing atomic volume so that the coordination polyhedra remain undistorted—in evident contrast to the collinear solution.

However, a closer inspection of the magnetic moments reveals a quite substantial difference compared to the model

proposed by Lawson *et al.*<sup>14</sup> We find (see Table IV) that the eight MnIIIb and MnIVb atoms split further into two subgroups labeled b1 and b2. Atomic positions within these subgroups are related through symmetry operations belonging to the  $D_{2d}$  space group. A splitting of the MnIII and MnIV sites

into more than two subgroups each was also postulated by Yamagata and Asayama<sup>16</sup> on the basis of their NMR data and explained in terms of the admixture of a second vector basis function to the representation of the magnetic moments. However, one must not forget that this analysis and the symmetry analysis of Yamada<sup>45</sup> are based on the assumption that the symmetry of the underlying crystal structure is cubic and hence the basis functions of the irreducible representations of the cubic space group have been used. From Table IV we learn that the moments on the b1 and b2 subgroups differ in orientation, but show almost no difference in the magnitude in the magnetic moments. We have also investigated whether the reduction of the magnetic symmetry is accompanied by a reduction of the crystalline symmetry. However, as already the tetragonal symmetry breaking was rather weak ( $c/a = 0.99955$ ), a further reduction of the crystalline symmetry could not be established at the given accuracy of our data.

In future it will be necessary to supplement our calculations by a group-theoretical analysis similar to that performed by Yamada. However, considering the fact that the voluminous study of Yamada dealt only with a possible noncollinear magnetic structure on a cubic crystalline lattice, this will require a substantial effort.

Finally we want to comment on the importance of using an unconstrained vector-field description of the magnetization density. We have found that while the noncollinear TB-LMTO calculations with fixed spin-quantization axes within the atomic spheres fails to find a stable noncollinear solution, such a structure is found in the unconstrained vector-field description implemented within the PAW. After the analysis of the spin-wave ground state<sup>61,62</sup> in  $\gamma$ -Fe, this is a further example for the importance of intra-atomic noncollinearity. Another example where atomic-sphere based and unconstrained description lead to different results are antiferromagnetic Cr and Mn monolayers on Cu(111) substrates. For Mn/Cu(111) it was found that while TB-LMTO-ASA calculations<sup>69</sup> predict a noncollinear Néel ground state with  $\sqrt{3} \times \sqrt{3}$  periodicity, unconstrained vector-field descriptions based on either the PAW (Ref. 70) or the FLAPW method<sup>71</sup> lead to the conclusion that a row-wise antiferromagnetic structure with  $c(2 \times 2)$  periodicity is preferred. For these simple two-dimensional structures it was also possible to visualize the vector field of the magnetization density and to explicitly demonstrate the intra-atomic noncollinearities in the outer regions of the atomic spheres. For the much more complex  $\alpha$ -Mn structure such a visualization is hardly feasible.

### F. Mechanical properties

Mn has not only very unusual crystalline and magnetic structures, its bulk modulus is also significantly lower than that of its neighbors in the Periodic Table—in striking contrast to the variation of the strength of bonding with the filling of the  $d$  band suggesting a maximum for a half-filled band. The experimentally determined values of the bulk modulus show a very large scatter. The older experiments which are often still referred to in the literature report extremely low values  $B_0 = 60$  GPa (Bridgman, Ref. 72 as cited

by Kittel<sup>73</sup>),  $B_0 = 93$  GPa (Rosen, Ref. 74). The Bridgman data are based on static compression experiments up to a pressure of 10 GPa and have been performed on specimens containing up to 3% of impurities, Rosen performed ultrasonic experiments. More recent static compression experiments using diamond anvil cell data extending up to 42 GPa produced values of  $B_0 = 131$  GPa (Takemura *et al.*, Ref. 75) and  $B_0 = 137$  GPa (Môri, Ref. 76), respectively. The most recent compression data by Fujihisa *et al.*<sup>7</sup> extending up to 90 GPa lead to a still higher value of  $B_0 = 158$  GPa. Whereas Takemura *et al.* reported an anomalously high value for the pressure dependence of the bulk modulus ( $B'_0 = 6.6$ ), Fujihisa *et al.* derived a lower value of  $B'_0 = 4.6$  rather close to the range characteristic for other transition metals.

We have calculated the bulk modulus of  $\alpha$ -Mn by fitting our energy vs volume data to a Birch-Murnaghan<sup>77</sup> equation and to the “universal equation-of-state” proposed by Vinet *et al.*<sup>78</sup> Both fits agree on a value of  $B_0 = 188 \pm 10$  GPa for antiferromagnetic  $\alpha$ -Mn. This is slightly above the range covered by the experiments, the overestimate is due to the too small equilibrium volume. As expected from the energy vs volume data, nonmagnetic  $\alpha$ -Mn has a much higher bulk modulus of  $B_0 \sim 260$  GPa. Hence the outstanding softness of  $\alpha$ -Mn is clearly due to the strong volume dependence of the magnetic moments around the equilibrium volume and not directly related to the unusual crystal structure. Sliwko *et al.*<sup>26</sup> calculated a bulk modulus of  $B_0 = 139$  GPa at the experimental density, no information on the equilibrium density corresponding to their LSDA approach is given. Hence the results are not directly comparable, but for an expansion to the experimental value we estimate a bulk modulus very close to their value.

### V. ELECTRONIC STRUCTURE

The bonding properties and the magnetic character of the structurally and magnetically inequivalent Mn atoms are of course reflected in the local electronic structure. Figure 6 shows the total and angular-momentum decomposed electronic densities of states (DOS) of  $\alpha$ -Mn as calculated for the nonmagnetic and the collinear antiferromagnetic phase at equilibrium. These DOS calculations are based on a tetrahedron integration over a dense Monkhorst-Pack grid. The comparison with the calculations performed on a coarser grid allows us to conclude that the total energies are well converged. Around the Fermi level, the electronic spectrum is entirely dominated by the  $3d$  states.  $s$ -orbitals contribute to the tail at high binding energies and to the peak at about  $-4$  eV binding energy,  $p$  states merely produce a low, structureless background to the  $3d$ -DOS extending from  $-5$  eV up to  $E_F$ .

Surprisingly (in view of the large magnetic moments on most of the sites), the total spin-integrated DOS's of both phases are almost identical. Both are characterized by a DOS minimum just below the Fermi energy. This result is important for understanding the stability of the  $\alpha$  phase compared to the high-symmetry  $\gamma$  and  $\delta$  phases above the Néel temperature. Of course we do not suggest that the paramagnetic

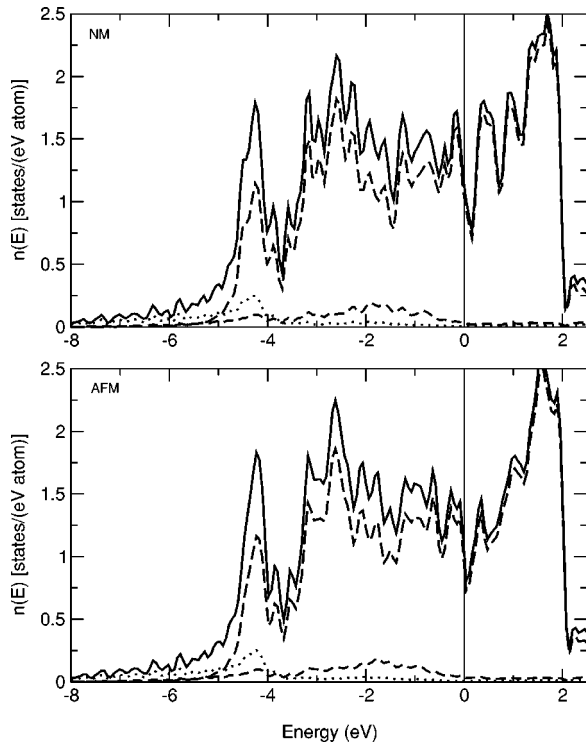


FIG. 6. Total (full lines) and  $s$ ,  $p$ ,  $d$ -decomposed (dotted, short- and long-dashed lines) electronic density of states for nonmagnetic (NM) and collinear antiferromagnetic (AFM) Mn, calculated at the equilibrium atomic volume.

local moments vanish completely above the Néel temperature—a disordered local-moment picture is certainly adequate for the paramagnetic state. However, within a mean-field description such as the DFT, the total electronic energy of the paramagnetic phase has to be calculated using the nonmagnetic DOS.

For the collinear antiferromagnetic phase we can decompose the local DOS's at the inequivalent sites into the majority- and minority-spin contributions, see Fig. 7. This analysis reflects the different character of the Mn atoms occupying the crystallographically inequivalent sites and reveals drastic differences in the local electronic structure and in the exchange splitting. While the DOS on the high-spin sites I and II is strongly structured and displays a deep minimum at the Fermi energy, those on sites III and IV show rather little structure. Essentially we can interpret the local variations in the electronic structure in terms of “magnetic impurity states” on sites I and II, immersed in a matrix of weakly magnetic or nonmagnetic MnIII and MnIV atoms.

On the MnI sites carrying the largest magnetic moments we find an almost completely filled majority  $d$  band and a strongly depleted minority band. In terms of the positions of the dominant peaks in the occupied majority-spin band and of the empty minority-spin band we estimate an exchange splitting of about  $\Delta_{\text{ex}} \sim 4.5$  eV. If the splitting is calculated in terms of the band centers, a somewhat smaller value of about 3.5 eV is obtained. From the ratio of magnetic moment and exchange splitting we obtain a value of the Stoner parameter of  $I = \Delta_{\text{ex}}/\mu \sim 1 \text{ eV}\mu_B^{-1}$  characteristic for itinerant

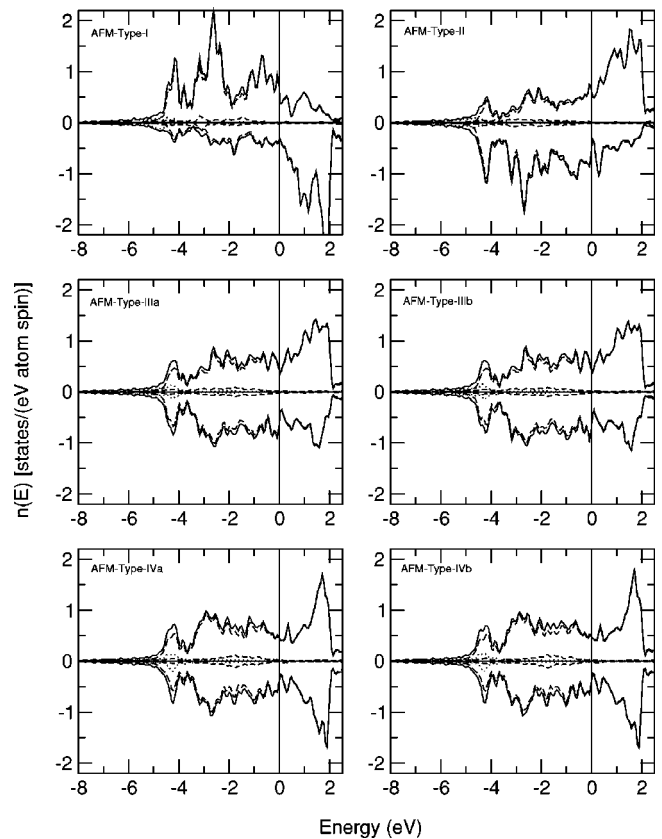


FIG. 7. Spin-polarized local densities of states on the crystallographically inequivalent sites in collinear antiferromagnetic Mn. Broken and dashed lines show the  $s$ ,  $p$ , and  $d$  components of the DOS.

magnets.<sup>79,80</sup> A similar conclusion can be drawn from the local spin-polarized DOS at sites II. Spin-polarization effects are much smaller on sites III and IV, but the positions of the band centers and the local magnetic moments are again compatible with an itinerant picture and a constant value of the Stoner parameter of  $I \sim 1 \text{ eV}\mu_B^{-1}$ . At the equilibrium volume, the magnetic moments on sites IV are essentially zero, spin-polarization effects in the DOS are absent. However, also for the low-spin sites the Fermi level is pinned in a minimum of the local DOS.

Compared to the ASW calculations of Sliwko *et al.*<sup>26</sup> our electronic structure shows more structure and a more pronounced exchange-splitting on sites I and II, but less structure on the weakly magnetic sites III and IV. These differences are clearly to be attributed to the use of the atomic-sphere approximation in the ASW calculations, with equal radii on all sites. For the  $\alpha$ -Mn structure this leads to large differences in the local overlap of the atomic spheres and the spherical averaging within the spheres tends to level the local variations in charge and spin densities. For this structure the atomic-sphere approximation is certainly a rather crude one.

The strong differences in the local DOS also lead to pronounced differences in the local magnetization densities and hence in the local magnetic form factor. This demonstrates that the previous analyses of the magnetic diffraction data based on the assumption of a magnetic form factor common

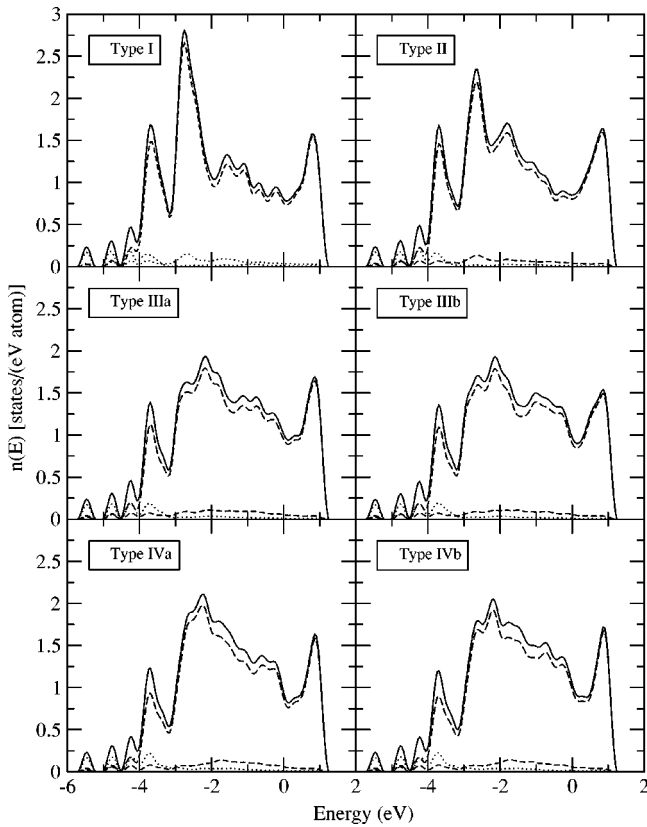


FIG. 8. Local densities of states on the crystallographically inequivalent sites in noncollinear antiferromagnetic Mn, calculated at a slightly expanded volume. For the symbols see Fig. 7.

to all sites must be considered only as first estimates and should be repeated with more realistic site-dependent form factors. However, the present plane-wave based calculations does not directly give us access to the individual atomic form factors—this could be achieved only via a projection onto local spin-dependent orbitals.

An analysis of the local DOS is more difficult for the noncollinear phase. Since the direction of the magnetization varies continuously throughout the lattice, it is not straightforward to define majority and minority components. Only an approximate definition based on magnetization directions averaged over atomic spheres would be possible. In addition, the computational effort associated with a noncollinear calculations forbids the use of a  $k$ -point mesh fine enough for a tetrahedron-integration and the extension of the calculations to excited states more than 1 eV above the Fermi energy. Hence only the spin-integrated DOS produced with Methfessel-Paxton smearing are reproduced in Fig. 8. These calculations have been performed for a slightly expanded volume of  $13 \text{ \AA}^3$  where appreciable transverse components of the magnetizations have been found on sites III and IV. The large volume lead to an overall reduction of the band width compared to the collinear results shown in Fig. 7. Compared to the collinear calculations the local DOS's on sites III and IV with canted magnetic moments show more pronounced minima at the Fermi level. This is clearly a consequence of the successful relief of the magnetic frustrations by the canting of the MnIII and MnIV moments and reflects

the stability of the noncollinear compared to the collinear structure.

## VI. SUMMARY AND CONCLUSIONS

Our study sheds an interesting light on the structural and magnetic complexity of Mn. We find that indeed—as proposed already many years ago—the ground state of  $\alpha$ -Mn may be interpreted as an intermetallic compound formed by Mn atoms of different size related to their magnetic properties. The crystal structure of  $\alpha$ -Mn shared with  $\chi$ -phase alloys (e.g.  $\text{Fe}_{36}\text{Cr}_{12}\text{Mo}_{10}$ ) and  $\gamma$ - $\text{Mg}_{17}\text{Al}_{12}$  is built by CN16 Friauf coordination polyhedra around the MnI and MnII sites carrying large magnetic moments. The MnIII and MnIV sites with smaller moments (and hence smaller diameters) have CN 13 and CN 12, with a local icosahedral symmetry around the MnIV sites. We have demonstrated that even in a non-magnetic phase this complex structure is at least locally stable—stability with respect to other crystal structures will be discussed in a following paper. Our results also explain the exceptional softness of  $\alpha$ -Mn—the low bulk modulus is a consequence of the rapid variation of the magnetic moments and the magnetic energies around equilibrium.

The tendency to form such a compact crystalline arrangement arises from the half-filled Mn- $d$  band—in the energetically favorable structure only bonding orbitals should be occupied and this leads to short interatomic distances. However, this strong-bonding tendency is in conflict with the tendency to maximize the magnetic spin moment according to Hund's rule. Strong bonding and short interatomic distances not only tend to quench the magnetic moment, for a metal where the nearest-neighbor exchange interaction is expected to be antiferromagnetic (as for all  $d$ -band elements with half or less-than-half filled bands), this also leads to a conflict with the local topology imposed by the close-packing requirement. As in the topologically close-packed polytetrahedral Frank-Kasper phases to which the A12 structure is closely related, the coordination polyhedra of  $\alpha$ -Mn have only triangular faces. On these faces antiferromagnetic coupling between nearest neighbors is necessarily frustrated. If the interatomic distances are short enough, the local moments are completely quenched. This happens for the CN16 polyhedron surrounding MnI for the twelve MnIV sites with a fivefold surface coordination. The four MnII sites with surface coordination six and a somewhat large distance from the center can form a large magnetic moment. The frustration arising from the formation of a magnetic moment on the MnIV sites can be relieved either by a large structural distortion or by a canting of the moments whose coupling is most strongly frustrated.

Our results are not in perfect agreement with experiment—even in the GGA, a certain tendency to overbinding exists so that at the theoretical equilibrium volume, the calculated magnetic structure is still collinear. However, a noncollinear structure develops at a slightly expansion. In this respect, the situation in Mn is similar to that in Cr where at the calculated equilibrium distance the antiferromagnetic moment is totally quenched<sup>21,22</sup> and where the magnetic moment shows critical behavior as a function of

volume—in evident analogy with the volume dependence of the MnIV moments. The noncollinear structure developing around the experimental density is similar to that proposed on the basis of the experimental data: large, almost collinear magnetic moments on sites I and II, substantially smaller and strongly canted moments on sites III and IV. However, a detailed comparison is difficult because the analysis of the data is based on assumptions (such as a magnetic form factor common to all Mn atoms) that are in contradiction to the calculated electronic structure and also in at least partial contradiction to the experiment itself.

The most important new aspect resulting from our study is a splitting of the MnIII and MnIV sites in three and not only in two magnetic subgroups (but no crystallographic splitting beyond that in two subgroups deduced from experiment). For the MnIV sites this can be related directly to the frustrated antiferromagnetic interactions in the small MnIV triangles on the surface of the CN16 Friauf polyhedron around MnI. The antiferromagnetic coupling leads to a local arrangement of the spins similar to that in the Néel phase of a frustrated triangular antiferromagnet. Whereas the spin directions on the MnIV-sites are almost independent of volume (and hence of the size of the MnIV moments), the volume dependent rotation of the MnIII moments out of their collinear orientations is driven essentially by the increasing frustration of the MnIII-MnIV coupling with increasing MnIV moments, mostly on the surface of the CN16 around the

MnII sites. A splitting into more than two magnetic subgroups has also been suggested on the basis of NMR experiments—but we do not find any sign for a splitting of the MnII sites into two magnetic subgroups. Such a splitting would lower the magnetic symmetry below  $D_{2d}$ , whereas the splitting of the MnIII and MnIV sites is still compatible with this space-group symmetry.

So far we have discussed only the  $\alpha$  phase of Mn. A forthcoming paper<sup>81</sup> will be devoted to the other polymorphs—their crystalline, magnetic, and electronic structures, their stability relative to the  $\alpha$  phase and to possible pressure-induced transitions between these phases. Without anticipating too much of these results, we only mention that the calculations predict the correct energetic order of the polymorphs at zero pressure ( $\alpha > \beta > \gamma$ ) and a pressure-induced transition from the  $\alpha$  phase to the hexagonal-close-packed  $\epsilon$  phase (confirming a still inconclusive interpretation of the high-pressure data).

#### ACKNOWLEDGMENTS

This work has been supported by the European TMR Network “Electronic Structure Calculations for Industry and Basic Sciences” (Contract No. ERB FMRX CT 98-0178) and by the Center for Computational Materials Science. Useful discussions with Georg Kresse are gratefully acknowledged.

- <sup>1</sup>J. Donohue, *The Structures of the Elements* (Wiley, New York, 1974).
- <sup>2</sup>R.S. Tebble and D.J. Craik, *Magnetic Materials* (Interscience, London, 1969).
- <sup>3</sup>A.J. Bradley and J. Thewlis, Proc. R. Soc. London, Ser. A **115**, 465 (1927).
- <sup>4</sup>G.D. Preston, Philos. Mag. **5**, 1207 (1928).
- <sup>5</sup>M. O’Keefe and S. Anderson, Acta Crystallogr., Sect. A: Cryst. Phys., Diffr., Theor. Gen. Crystallogr. **33**, 914 (1977).
- <sup>6</sup>Y. Endoh and Y. Ishikawa, J. Phys. Soc. Jpn. **30**, 1614 (1971).
- <sup>7</sup>H. Fujihisa and K. Takemura, Phys. Rev. B **52**, 13257 (1995).
- <sup>8</sup>J.X. Zheng-Johansson, O. Eriksson, B. Johansson, L. Fast, and R. Ahuja, Phys. Rev. B **57**, 10 989 (1998).
- <sup>9</sup>C.G. Shull and M.K. Wilkinson, Rev. Mod. Phys. **25**, 100 (1953).
- <sup>10</sup>J.S. Kasper and B.W. Roberts, Phys. Rev. **101**, 537 (1956).
- <sup>11</sup>J.A. Oberteuffer, J.A. Marcus, L.H. Schwartz, and G.P. Felcher, Phys. Lett. **28A**, 267 (1969).
- <sup>12</sup>N. Kunitomi, Y. Yamada, Y. Nakai, and Y. Fujii, J. Appl. Phys. **40**, 1265 (1969).
- <sup>13</sup>T. Yamada, N. Kunitomi, Y. Nakai, D.E. Cox, and G. Shirane, J. Phys. Soc. Jpn. **28**, 615 (1970).
- <sup>14</sup>A.C. Lawson, A.C. Larson, M.C. Aronson, S. Johnson, Z. Fisk, P.C. Canfield, J.D. Thompson, and R.B. Von Dreele, J. Appl. Phys. **76**, 7049 (1994).
- <sup>15</sup>T. Yamada and S. Tazawa, J. Phys. Soc. Jpn. **28**, 609 (1970).
- <sup>16</sup>H. Yamagata and K. Asayama, J. Phys. Soc. Jpn. **33**, 400 (1972).
- <sup>17</sup>L. Brewer, Science **161**, 115 (1968).
- <sup>18</sup>H. Nakamura, K. Yoshimoto, M. Shiga, M. Nishi, and K. Kaku-  
rai, J. Phys.: Condens. Matter **9**, 4701 (1997).
- <sup>19</sup>B. Canals and C. Lacroix, Phys. Rev. B **61**, 11 251 (2000).
- <sup>20</sup>E.G. Moroni, G. Kresse, J. Hafner, and J. Furthmüller, Phys. Rev. B **56**, 15 629 (1997).
- <sup>21</sup>H. Zabel, J. Phys.: Condens. Matter **11**, 9303 (1999).
- <sup>22</sup>R. Hafner, D. Spišák, R. Lorenz, and J. Hafner, J. Phys.: Condens. Matter **13**, L239 (2001); Phys. Rev. B **65**, 184432 (2002).
- <sup>23</sup>T. Asada and K. Terakura, Phys. Rev. B **47**, 15 992 (1993).
- <sup>24</sup>M. Eder, J. Hafner, and E.G. Moroni, Phys. Rev. B **61**, 11 492 (2000).
- <sup>25</sup>T. Oguchi and A.J. Freeman, J. Magn. Magn. Mater. **46**, L1 (1984).
- <sup>26</sup>V. Sliwko, P. Mohn, and K. Schwarz, J. Phys.: Condens. Matter **6**, 6557 (1994).
- <sup>27</sup>V.P. Antropov, M. van Schilfgaarde, and B.N. Harmon, J. Magn. Magn. Mater. **140-144**, 1355 (1995).
- <sup>28</sup>T. Asada, J. Magn. Magn. Mater. **140-144**, 47 (1995).
- <sup>29</sup>F. Süß and U. Krey, J. Magn. Magn. Mater. **125**, 351 (1993).
- <sup>30</sup>D. Vanderbilt, Phys. Rev. B **41**, 7892 (1990).
- <sup>31</sup>G. Kresse and J. Hafner, J. Phys.: Condens. Matter **6**, 8245 (1994).
- <sup>32</sup>P.E. Blöchl, Phys. Rev. B **50**, 17 953 (1994).
- <sup>33</sup>G. Kresse and D. Joubert, Phys. Rev. B **59**, 1758 (1999).
- <sup>34</sup>A recent example is the optimization of the crystal structure of mordenite, an aluminosilicate with 144 atoms per unit cell. See Th. Demuth, J. Hafner, L. Benco, and H. Toulhoat, J. Phys. Chem. B **104**, 4593 (2000).
- <sup>35</sup>G. Kresse and J. Hafner, Phys. Rev. B **48**, 13 115 (1993); **49**, 14 251 (1994); **55**, 5364 (1997).

- <sup>36</sup>K. Seifert-Lorenz and J. Hafner, Phys. Rev. B **59**, 829 (1999); **59**, 843 (1999).
- <sup>37</sup>J. Kübler, K.H. Höck, and J. Sticht, J. Appl. Phys. **63**, 3482 (1988).
- <sup>38</sup>R. Lorenz and J. Hafner, J. Magn. Magn. Mater. **139**, 209 (1995); R. Lorenz, J. Hafner, S.S. Jaswal, and D.J. Sellmyer, Phys. Rev. Lett. **74**, 3688 (1995).
- <sup>39</sup>E. Wimmer, H. Krakauer, M. Weinert, and A.J. Freeman, Phys. Rev. B **24**, 864 (1981); M. Weinert, E. Wimmer, and A.J. Freeman, *ibid.* **26**, 4571 (1982).
- <sup>40</sup>T. Asada, G. Bihlmayer, S. Handschuh, S. Heinze, Ph. Kurz, and S. Blügel, J. Phys.: Condens. Matter **11**, 9347 (1999).
- <sup>41</sup>L. Nordström and D.J. Singh, Phys. Rev. Lett. **76**, 4420 (1996).
- <sup>42</sup>D. Hobbs, G. Kresse, and J. Hafner, Phys. Rev. B **62**, 11 556 (2000).
- <sup>43</sup>W.B. Pearson, *The Crystal Physics and Chemistry of Metals and Alloys* (Wiley, New York, 1972).
- <sup>44</sup>A. Arrott, B.R. Coles, and J.E. Goldman, Phys. Rev. **98**, 1864 (1955); A. Arrot and B.R. Coles, J. Appl. Phys. **32**, 515 (1961).
- <sup>45</sup>T. Yamada, J. Phys. Soc. Jpn. **28**, 596 (1970).
- <sup>46</sup>F. Bertaut, in *Magnetism*, edited by G.T. Rado and H. Suhl (Academic Press, New York, 1963), Vol. III, p. 149.
- <sup>47</sup>A.V. Shubnikov and N.V. Belov, *Coloured Symmetry* (Wiley, New York, 1964), p. 198.
- <sup>48</sup>A.J. Freeman and R.E. Watson, Acta Crystallogr. **14**, 231 (1961).
- <sup>49</sup>A.R. Williams, J. Kübler, and C.D. Gelatt, Phys. Rev. B **19**, 6094 (1979).
- <sup>50</sup>O. Gunnarson, O. Jepsen, and O.K. Andersen, Phys. Rev. B **27**, 7144 (1983).
- <sup>51</sup>O.K. Andersen, O. Jepsen, and D. Götzel, in *Highlights of Condensed Matter Theory*, edited by F. Fumi and M.P. Tosi (North Holland, New York, 1985); O.K. Andersen, D. Jepsen, and M. Šob, in *Electronic Band Structure and its Applications*, edited by M. Youssouff (Springer, Berlin, 1987).
- <sup>52</sup>D.A. Papaconstantopoulos, *Handbook of the Band-Structure of Elemental Solids* (Plenum, New York, 1986).
- <sup>53</sup>S.G. Louie, S. Froyen, and M.L. Cohen, Phys. Rev. B **26**, 1738 (1982).
- <sup>54</sup>U. von Barth and L. Hedin, J. Phys. C **5**, 1629 (1972).
- <sup>55</sup>J. Kübler, K.H. Höck, J. Sticht, and A.R. Williams, J. Phys. F: Met. Phys. **18**, 469 (1988).
- <sup>56</sup>L.M. Sandratskii and P.G. Guletskii, J. Phys. F: Met. Phys. **16**, L43 (1986).
- <sup>57</sup>J.P. Perdew and A. Zunger, Phys. Rev. B **23**, 5048 (1981).
- <sup>58</sup>D.M. Ceperley and B.J. Alder, Phys. Rev. Lett. **45**, 566 (1980).
- <sup>59</sup>J.P. Perdew, J.A. Chevary, S.H. Vosko, K.A. Jackson, M.R. Pederson, D.J. Singh, and C. Fiolhais, Phys. Rev. B **46**, 6671 (1992).
- <sup>60</sup>J.A. White and D.M. Bird, Phys. Rev. B **50**, 4954 (1994).
- <sup>61</sup>K. Knöpfle, L.M. Sandratskii, and J. Kübler, Phys. Rev. B **62**, 5564 (2000).
- <sup>62</sup>M. Marsman and J. Hafner, Phys. Rev. B **66**, 224409 (2002).
- <sup>63</sup>G. Kresse and J. Furthmüller, Phys. Rev. B **54**, 11 169 (1996).
- <sup>64</sup>G. Kresse and J. Furthmüller, Comput. Mater. Sci. **6**, 15 (1996).
- <sup>65</sup>The Vienna LMTO package has been programed by D. Spišák.
- <sup>66</sup>P. Pulay, Chem. Phys. Lett. **73**, 393 (1980).
- <sup>67</sup>H.J. Monkhorst and J.D. Pack, Phys. Rev. B **13**, 5188 (1976).
- <sup>68</sup>G. Bihlmayer, T. Asada, and S. Blügel, Phys. Rev. B **62**, 11 937 (2000).
- <sup>69</sup>D. Spišák and J. Hafner, Phys. Rev. B **61**, 12 728 (2000).
- <sup>70</sup>D. Hobbs and J. Hafner, J. Phys.: Condens. Matter **12**, 7025 (2000); D. Spišák, D. Hobbs, and J. Hafner, Phys. Rev. B **63**, 096402 (2001).
- <sup>71</sup>T. Asada, G. Bihlmayer, S. Handschuh, S. Heinze, Ph. Kurz, and S. Blügel, J. Phys.: Condens. Matter **11**, 9347 (1999); Ph. Kurz, G. Bihlmayer, S. Blügel, K. Hirai, and T. Asada, Phys. Rev. B **63**, 096401 (2001).
- <sup>72</sup>P.W. Bridgman *Collected Experimental Papers* (Harvard University Press, Cambridge, MA, 1964).
- <sup>73</sup>C. Kittel *Introduction to Solid State Physics* (Wiley, New York, 1976).
- <sup>74</sup>M. Rosen, Phys. Rev. **165**, 357 (1968).
- <sup>75</sup>K. Takemura, O. Shimomura, K. Hase, and T. Kikegawa, J. Phys. F: Met. Phys. **18**, 197 (1988).
- <sup>76</sup>N. Mōri, M. Takahashi, and G. Oomi, J. Magn. Magn. Mater. **31-34**, 135 (1983).
- <sup>77</sup>F.D. Murnaghan, Proc. Natl. Acad. Sci. U.S.A. **3**, 244 (1944).
- <sup>78</sup>P. Vinet, J.R. Smith, J. Ferrante, and J.H. Rose, Phys. Rev. B **35**, 1945 (1987).
- <sup>79</sup>I. Turek, Ch. Becker, and J. Hafner, J. Phys.: Condens. Matter **4**, 7257 (1992).
- <sup>80</sup>F.J. Himpsel, Phys. Rev. Lett. **67**, 2363 (1991).
- <sup>81</sup>J. Hafner and D. Hobbs, following paper, Phys. Rev. B **68**, 014408 (2003).